International Journal of Multiphase Flow 168 (2023) 104581

Contents lists available at ScienceDirect

International Journal of Multiphase Flow

journal homepage: www.elsevier.com/locate/ijmulflow

Combined optical connectivity and optical flow velocimetry measurement of interfacial velocity of a liquid jet in gas crossflow

Tianyi Wang *, Yannis Hardalupas

Imperial College London, Mechanical Engineering Department, London, SW7 2AZ, United Kingdom

A R T I C L E I N F O

Keywords:
Optical connectivity
Optical flow velocimetry
Interfacial motion
Liquid jet in crossflow
Atomisation

A B S T R A C T

Liquid jet in crossflow (LJIC) is a process in which a high-speed gas crossflow deforms and shears a continuous liquid flow into tiny droplets. This study quantifies the liquid surface motion of LJIC during the primary breakup process, which has not been quantified due to the optical limitation close to the nozzle exit. The interfacial velocity of a breaking liquid jet indicates the local interaction of the gas and liquid flows and determines the initial velocity of the stripped droplets. The local interfacial liquid velocities of LJIC have only been estimated from theoretical and computational studies, which have not been evaluated from measurements. Optical Connectivity (OC) introduces a laser beam through an atomiser nozzle and relies on total internal reflection at the liquid interface to propagate the laser light inside the continuous liquid to record the instantaneous features of the interface of the continuous liquid during the primary atomisation at the near nozzle region through imaging of the emitted fluorescent intensity from the liquid flow. The current study combines Optical Connectivity with Optical Flow Velocimetry (OFV) to quantify the time-dependent, local interfacial velocity of the liquid interface structures of the LJIC for gas Weber numbers between 14.9 - 112.6 and liquid-to-gas momentum ratios between 2.1 - 36.4. The combined OC-OFV measurements of the spatial distribution of the mean and fluctuating values of the different components of the liquid interfacial velocity of LJIC demonstrate how the gaseous shear and liquid jet geometry interact to influence the atomisation process.

1. Introduction

A liquid stream injected into high-speed gaseous crossflow, referred as a liquid jet in crossflow (LJIC), has been studied for several applications, such as blade cooling, agriculture spray and fuel atomisation in combustors (Ghosh and Hunt, 1998; Mahesh, 2013; Wu et al., 1997). For liquid-fuel combustion devices, LJIC has been utilized to potentially enhance combustion efficiency and reduce pollutant emissions due to the atomisation characteristics of the LJIC. A more controllable penetration and distribution of the stripped-off fuel droplets from the liquid jet can be achieved by carefully adjusting the relevant parameters, while a uniform air-fuel mixture ratio is also generated by LJIC, owing to the complex gas flow structures surrounding the injected liquid jet such as counter-rotating vortex pairs (CVP) (Behzad et al., 2016; Elshamy et al., 2006; Kelso et al., 1996; Li and Soteriou, 2016; X. 2018; Lubarsky et al., 2010; Wu et al., 1998). The different breakup regimes have been shown to depend on the gaseous Weber number We_G, momentum flux ratio M, gaseous and liquid Reynold number (Re_G and Re_L) and Ohnesorge number Oh (Mazallon et al., 1999; Ng et al., 2008; Sallam et al., 2004, 2002; Wu et al., 1997). which are defined and discussed further in Section 2. However, the physics of the primary breakup are not fully understood. A study of the primary breakup of LJIC that quantifies the characteristics of the disintegrating interfacial features and their local velocity is required to obtain new insight on droplet formation, resulting droplet sizes and spatial distribution of the downstream spray.

A challenge in the measurement of the primary breakup of LJIC is the dense droplet clouds surrounding the liquid core, which limit optical access to the interfacial features and geometry of the continuous liquid core, especially for the multimode and shear breakup regimes for which the surface breakup dominates the atomisation process (Mazallon et al., 1999; Sallam et al., 2004; Wu et al., 1997). During the primary breakup of LJIC, the gas flow shear at the interface and the resulting gas flow vortical structures, formed in the wake of the liquid jet, destabilise the liquid surface and strip droplets, some of which can be carried upstream of the liquid jet region, as measured by Particle Image Velocimetry (PIV) and Phase Doppler Particle Analyser (PDPA) and demonstrated by simulations (Behzad et al., 2016; Elshamy et al., 2006; Li and Soteriou, 2016; Lubarsky et al., 2010). However, such measurements were mainly

* Correspondent author.
E-mail address: tw5017@ic.ac.uk (T. Wang).

https://doi.org/10.1016/j.ijmultiphaseflow.2023.104581
Received 13 February 2023; Received in revised form 28 May 2023; Accepted 17 July 2023
Available online 19 July 2023

performed further away from the breakup region where the liquid concentration is reduced. Shadowgraphic techniques have been used to image the liquid breakup region, but could only capture the breakup of liquid jets with less complex breakup features, such as those present under column and bag breakup regimes (Ng et al., 2008). Meanwhile, the liquid jet break regimes that lead to improved atomisation cause higher optical depth and the breakup features, such as breakup length and liquid penetration trajectory, can vary significantly (Mohsen Broumand and Birouk, 2016).

To subside the optical attenuation of illuminating light and multiple scattering effects from the dense droplet clouds around the liquid core at the breakup region, which limit shadowgraphic imaging, ballistic imaging was developed to observe the breakup region at the near-field of atomisers (Linne et al., 2005). Nevertheless, this method has not been broadly applied to study the breakup process physics in LJIC. The Optical Connectivity (OC) was proposed by Charalampous et al. (2007) to avoid or limit the influence from the surrounding droplets in order to study the breakup physics of air-assisted atomisation. Besides, Wang and Hardalupas (2021) combined the Optical Flow Velocimetry (OFV) and Optical Connectivity (OC) [OC-OFV], to quantify the interfacial velocity along the surface of a continuous liquid jet injected by a pressure jet atomiser into quiescent air. This technique measured the detailed distribution of interfacial velocities on the liquid surface and revealed the significance of liquid viscosity and liquid shear layer on the atomisation process.

The current study applies both OC and shadowgraphy to study the breakup features during primary breakup of LJIC and compares the results from both techniques for three breakup regimes, namely bag breakup, multimode breakup and shear breakup. Then, the Optical Flow Velocimetry (OFV) is combined with OC to measure the local interfacial velocities of the liquid interface structures of the LJIC and demonstrate the information that can be extracted by such measurements. The interfacial velocity distribution along the 3-D geometry of the liquid core of LJIC is quantified for the first time and provides new information of liquid jet breakup and the influence of surrounding gas flow structures on the liquid jet interfacial velocity. The paper is structured as follows. Section 2 describes the experimental arrangement, flow operating conditions and the image analysis and uncertainties. This section also includes a review of the previous findings on LJIC in order to explain the selected operating flow conditions. Section 3 presents and discusses the spatial development of the interfacial velocity of the liquid jet at different locations and flow conditions. The paper ends with a summary of the main findings.

2. Experimental arrangement and methodology

2.1. Atomisation facility of liquid jet in crossflow (LJIC) and flow operating conditions

The specially designed axisymmetric atomiser of the current study is presented in Fig. 1. The main body of the atomiser was set vertically and designed with four radial inlets which are mounted at the far end of a cylindrical plenum chamber to allow the gas flow supply to the nozzle after flowing through a mounted straightener which is applied to prevent the generation of turbulence in the gas flow. In addition, the length of the development of the boundary layer on the liquid tube surface is short after the contraction to allow the growth of a turbulent boundary layer. Therefore, it is expected that the gas boundary layer remains thin at the location of the interaction with the liquid jet. A more detailed description of the atomiser can be found in Hadjiyiannis (2014). The cylindrical chamber with diameter 90 mm was closed at the far end by a plate and, at the other side, was connected to a conical contraction with 38 mm exit diameter to accelerate the gas flow. The contraction ended in a straight nozzle and was extended by a straight glass tube, which was used to confine the gas flow from the contraction exit. Moreover, the glass tube allowed the light source of optical techniques to illuminate the gas and liquid flows and ensured the application of both Optical Connectivity and Shadowgraphic techniques. It is within the length of the glass tube that the atomisation of the injected liquid jet takes place and can be studied, while the surrounding air flow velocity remains constant. A main difference between the current atomiser and those of previous studies is that the atomiser allows uniform axisymmetric gas

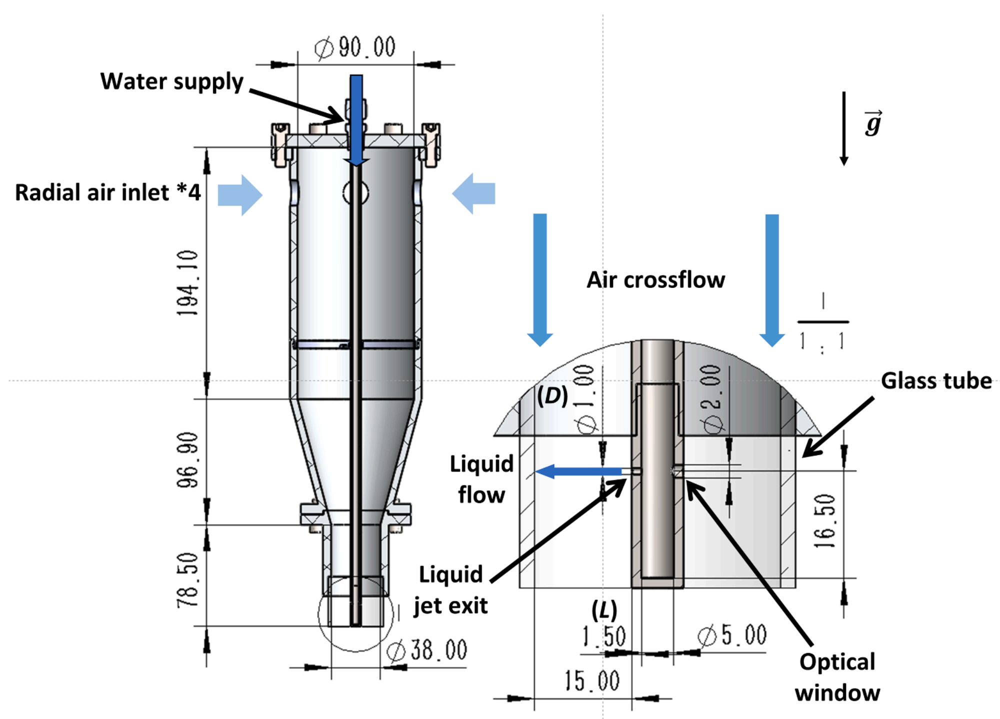

Fig. 1. Schematic of atomizer of liquid jet exposed to a cross stream of air (elevation view). Detail at bottom right shows design of liquid nozzle exit and optical window.

flow to interact with a liquid jet injected normally to the gas flow, as happens in many applications.

The liquid was supplied through a long straight stainless-steel tube of circular cross-section with 5 mm internal and 8 mm external diameter (more detail in Fig. 1). This delivering tube was supported along the centreline of the atomiser main body and was connected to the liquid supply at one end. The other end of the delivering tube was closed and a circular hole with diameter of 1 mm was drilled at the side of the tube normal to its centreline at the start of the transparent glass tube. In this way, a liquid jet could be injected normally to the gas flow within the bounds of the transparent glass tube, which allows the study of LJIC. Therefore, the length to diameter ratio, *L/D,* of the injecting liquid nozzle is 1.5, while the annular gap between the central liquid-delivering tube and the outer glass tube was 15 mm. For the implementation of the optical connectivity technique, an optical window was placed on the liquid-delivering tube right opposite of the liquid exit, as shown in the detail at the bottom right of Fig. 1. The transparent glass tube of the gas flow annulus provided direct optical access to the optical window at the back of the liquid injection orifice. A laser beam could therefore be directed into the liquid jet to allow the application of the OC technique. In the current study, Rhodamine B was mixed in the supplied water with concentration of 5×10^{-7} mol/L and injected into the high-speed air crossflow through the 1 mm diameter orifice. The LED light source of shadowgraphy technique, at the same time, can also illuminate the liquid jet flow through the transparent glass tube. The air and liquid flow rates are controlled by rotameters.

Several non-dimensional parameters affect the characteristics of the crossflow atomisation, which determine the breakup regimes, liquid breakup length and spray droplet size distribution (Mazallon et al., 1999; Ng et al., 2008; Sallam et al., 2004; Wu et al., 1997). The relevant non-dimensional parameters include: (i) gas Weber number $We_G = \rho_G V_G^2 D/\sigma$, (ii) liquid-to-gas momentum flux ratio $M = \rho_L U_L^2 / \rho_G V_G^2$, (iii) Ohnesorge number $Oh = \mu_L/\sqrt{\rho_L D\sigma}$, (iv) gas Reynolds number $Re_G = \rho_G V_G D/\mu_G$ and (v) liquid Reynolds number $Re_L = \rho_L U_L D/\mu_L$. These parameters have been reported to affect or determine the breakup features of the LJIC (Birouk et al., 2003;Broumand and Birouk, 2016;Broumand and Birouk, 2019; Ng et al., 2008; Osta and Sallam, 2007; Sallam et al., 2004; Sallam et al., 2006; Wu et al., 1998). The notations at the above non-dimensional parameters are: diameter of the injection orifice D, density of crossflow gas ρ_G, density of injected liquid ρ_G, liquid and gas viscosity μ_L and μ_G, and liquid surface tension σ. The liquid and gas properties remain constant, as shown in Table 1, and the liquid nozzle diameter D is equal to 1 mm. Therefore, by varying the crossflow gas velocity V_G, the We_G number can be controlled to access different breakup regimes while the liquid velocity U_L is kept constant.

The breakup regime map suggested by Sallam et al. (2004), given in Fig. 2, is used to guide the operating flow conditions and define the breakup regimes. In addition, due to the low value of L/D of the injecting nozzle, the initial injected liquid jet is expected to have a nearly uniform liquid velocity profile with a very thin boundary layer close to the wall. Therefore, the liquid velocity profile will be developing downstream of the nozzle exit. Five gas flowrates, shown in Table 2, are considered in the current study and are marked on the regime map of Fig. 1 to indicate the relevant breakup regime. The first gas flowrate ($V_G = 29.8$ m/s) falls in the bag breakup regime ($4 < We_G < 30$) where the breaking bag structures can be clearly observed (Lubarsky et al., 2012; Ng et al., 2008), and the gas flowrate with the maximum V_G (gas flow 5) is dominated by strong surface stripping and falls in the shear breakup regime ($We_G > 110$) (Sallam et al., 2004; Wu et al., 1997). The rest three

Table 1
Properties of gas and liquid fluids.

$\rho_G (kg/m^3)$	$\rho_L (kg/m^3)$	$\mu_L (pa\cdot s)$	$\mu_G (pa\cdot s)$	$\sigma (N/m)$
1.225	997	8.90×10^{-4}	1.85×10^{-5}	7.28×10^{-2}

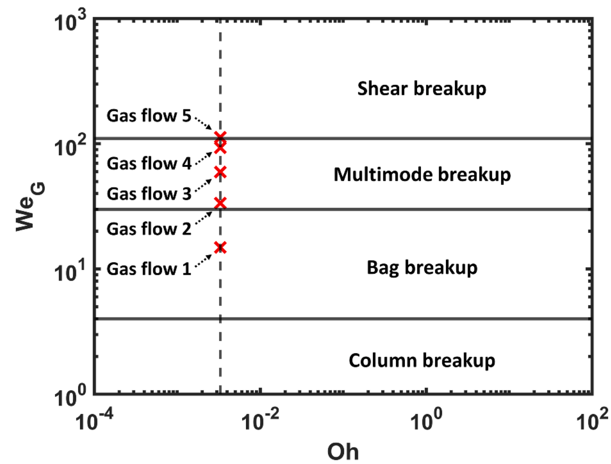

Fig. 2. Breakup regime map of LJIC suggested by Sallam et al. (2004).

gas flowrates are in the multimode breakup regime ($30 < We_G < 110$) where both the bag breakup and surface stripping coexist, while the competition between bag and surface breakup leads to a breaking jet with more complex features. Moreover, the liquid jet trajectory and maximum penetrating length are mainly influenced by the momentum flux ratio M, which is varied by the gas crossflow velocity V_G and liquid jet velocity U_L. To evaluate the effect of M on the breakup characteristics, three different values of U_L (4.2 m/s, 5.3 m/s and 6.4 m/s) were considered and all the flow cases are separated into three groups as shown in Table 2. Each group has flow conditions, where the liquid jet is introduced with a constant U_L, but V_G is varied. In this way, for the same V_G, We_G number is identical for different groups, while the magnitude of M increases from group 1 to group 3. The liquid and gas Reynolds numbers Re_L and Re_G are also considered as influential factors, since the liquid jet turbulence has been suggested that modifies the boundaries of the breakup regimes (Lee et al., 2007; Sallam et al., 2002, 2006) and the gas flow conditions may also affect the dominant mode of the interfacial instabilities (Arienti and Soteriou, 2009; Li and Soteriou, 2016; X. 2018; Ng et al., 2008). Table 1 and Table 2 list the physical properties of the fluids and the non-dimensional parameters of the considered flow conditions respectively.

2.2. Optical arrangement and coordinate system

Fig. 3(a) shows a plan view of the optical arrangement for carrying out optical connectivity (OC) and shadowgraphy imaging techniques respectively. A nanosecond Nd:YAG laser (New Wave Research, Solo 120), operating at 532 nm wavelength, is used as the illumination source for OC. The typical pulse duration and maximum pulse energy of the laser are 4 ns and 75 mJ. A laser beam with initial 6 mm diameter is introduced into the liquid jet nozzle through the optical window after appropriate adjustments by lenses. A LED light source transmitted light normal to the axis of the liquid jet for shadowgraphic imaging. By separately imaging with OC and shadowgraphy, the effects of the cloud of the surrounding droplets on the primary breakup features could be analysed, while the relevant breakup characteristics can be quantified by suppressing the influence of the droplets surrounding the liquid core with the OC technique. The side-view images of the disintegrating liquid jet are captured from a PCO Sensicam QE inter-frame CCD camera (12 bit, 1040 × 1376 pixels) with SIGMA lens with 105 mm focal length and f-number 2.8 (see Fig. 3(a)). Since Rhodamine B dissolved in water absorbs laser light at 532 nm and emit fluorescence with peak wavelength at around 575 nm at room temperature (Seuntiëns et al., 2001), a Schott OG 550 long pass optical filter was mounted in front of the lens to remove the illuminating green laser light and any other undesirable light. Fig. 3(b) presents the coordinate system with the elevation view

Table 2
Non-dimensional parameters of considered flow cases.

Group	U_L (m/s)	Gas Flow No.	V_G (m/s)	We_G	M	Re_G	Re_L	Oh	Breakup Regime
1	4.2	1	29.8	14.9	16.1	1973	4677	3.3×10^{-3}	Bag
		2	44.7	33.6	7.2	2960			Multimode
		3	59.5	59.6	4.1	3940			Multimode
		4	74.4	93.1	2.6	4926			Multimode
		5	81.8	112.6	2.1	5417			Shear
2	5.3	1	29.8	14.9	25.7	1973	5937		Bag
		2	44.7	33.6	11.4	2960			Multimode
		3	59.5	59.6	6.5	3940			Multimode
		4	74.4	93.1	4.1	4926			Multimode
		5	81.8	112.6	3.4	5417			Shear
3	6.3	1	29.8	14.9	36.4	1973	7057		Bag
		2	44.7	33.6	16.2	2960			Multimode
		3	59.5	59.6	9.1	3940			Multimode
		4	74.4	93.1	5.8	4926			Multimode
		5	81.8	112.6	4.8	5417			Shear

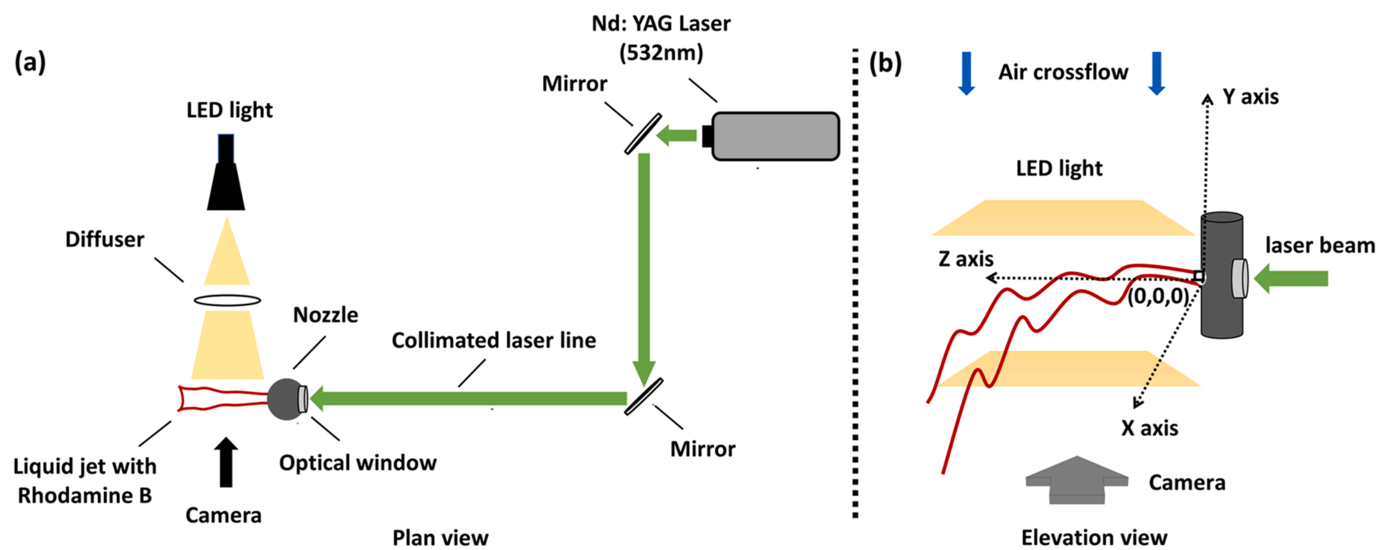

Fig. 3. Optical arrangements for the optical connectivity and shadowgraphy techniques; (a) plan view (b) elevation view.

used in the current study. The origin of the coordination system is set at the centre of the liquid jet nozzle exit. *Z*-axis is prescribed to depict the streamwise direction of the liquid jet, which can be used to indicate the penetration distance of the liquid jet from the nozzle exit. *Y*-axis is set along the air crossflow direction, which is perpendicular to *X*-axis. The camera is set along the *X*-axis, while the laser source for OC is guided through the liquid jet along the *Z*-axis and the LED light source is directed along the *X*-axis. The physical dimension of the recorded images is about 8.7 mm x 6.6 mm, resulting in a spatial resolution of around 6.3 μm/pixel.

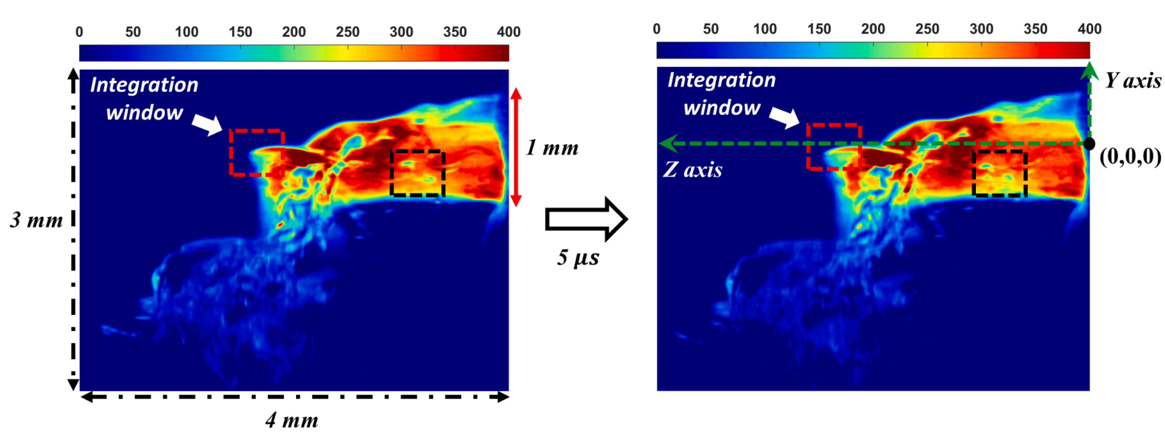

Fig. 4. Two OC fluorescent intensity images of the liquid jet in crossflow recorded by the camera with interval time 5 μs. Two example interrogation windows are shown on the images, which allow the application of Optical Flow Velocimetry (OFV) algorithms to measure the local velocity of the liquid interface structures.

2.3. Combined optical connectivity (OC) and optical flow velocimetry (OFV)

The fluorescent intensity emitted from the liquid jet core, as shown in Fig. 4, can be captured by OC which shows the instantaneous windward surface waves (the red windows in Fig. 4). Meanwhile, due to the complex refraction of the light caused by surface deformations, the stripping-off structures at the edge of the liquid core (the black windows in Fig. 4) can also be observed based on the fluorescent intensity. The refraction of the fluorescent light at the interface causes spatial and temporal fluorescent intensity variations due to 'caustics' at the liquid interface which can indicate the locations of deformation on the interface. The cross-correlation of the fluorescent intensity distribution between subsequent images in time, similar to that performed by PIV algorithms, can be used to quantify the displacement of these local fluorescent intensity variations. A smooth liquid interface has uniform fluorescent intensities and, therefore, no distinct peak can be found in the corresponding correlation plane and the computed vector is rejected by strict peak ratio. This tracing approach is known as Optical Flow Velocimetry (OFV) or Image Correlation Velocimetry (ICV), which has been applied to measure the velocity of variable scalar field, such as local flame and stripped-off droplets during atomisation (Charalampous and Hardalupas, 2016; Fielding et al., 2001; Komiyama et al., 1996; Sedarsky et al., 2009, 2013; Tokumaru and Dimotakis, 1995). For a liquid jet injected into a quiescent air, Wang and Hardalupas (2021) developed a combined OC-OFV method, bringing together the strengths of both OC and OFV, to quantify the local interfacial liquid velocities by tracking the emitted fluorescent intensity from deformations of the liquid interface. In the context of LJIC, Ng et al. (2008) proposed a similar block tracking method to measure the velocity of the windward surface wave from time-delayed image recordings from double-pulsed shadowgraphy technique, which is also analogous to OFV method. However, while their approach can measure the windward interfacial velocity, the stripping characteristics close to the nozzle exit or at the edge of the liquid core cannot be quantified by the shadowgraphy technique. Therefore, the combined OC and OFV technique (OC-OFV) of the present study is used to measure the motion of windward surface waves and the stripping-off structures at the edge of the liquid core and quantify the instantaneous interfacial velocity vector maps of the LJIC. More details on OC-OFV can be found in Wang and Hardalupas (2021). Besides, the low magnitude of U_L and the fluorescent intensity images captured by OC indicate that no cavitation is present in the liquid flow inside the nozzle for all the tested conditions. The presence of bubbles inside the liquid jet would distort the fluorescence emitted from the liquid core and disturb the uniformity of the fluorescent intensity close to the nozzle exit, which is not observed.

The double pulse laser operating at 532 nm was used with interval time between the pulses of 5 μs for all flow cases of Table 2 to generate time-delayed pairs of OC images. The fluorescent intensity in the interrogation window of Fig. 4 was traced by a cross-correlation algorithm to calculate the displacement of the intensity pattern, which can then estimate the interfacial velocity on the liquid jet. The LaVision PIV software (Davis 8) was used to compute the interfacial velocity and a multi-step cross-correlation algorithm was applied to the captured images. This algorithm used first a coarse interrogation window of 256 × 256 pixels with 50% window overlap to trace the movement of larger fluorescent intensity patterns. After capturing the movement of the larger scales, a refined interrogation window of 32 × 32 pixels with 75% window overlap is used to quantify the movement of the smaller scales that are present within the first interrogation window. Therefore, the smallest resolved liquid flow structure is around 201.6 μm, while adjacent velocity vectors have a separation distance of 8 pixels (around 50.4 μm). A strict median filter and peak ratio were applied to reject spurious vectors. It is worth mentioning that a long interval time between the laser pulses is not recommended, since the geometry of the interfacial features may change significantly and the cross-correlation algorithm cannot identify the interfacial motion. Details of this cross-correlation algorithm can be found in Adrian et al. (2011), Raffel (2018).

OFV velocity measurements of the LJIC interfacial structures is based on 1500 pairs of OC fluorescent intensity images. Only flow cases with faster gas velocity (gas flow 3, 4 and 5) are analysed by OFV, since more surface deformations are present for these cases, particularly at the region close to the nozzle exit (see Fig. 4). In the current study, the OFV measurement was applied to the captured images with the coordinate system of Fig. 4. The axial component (parallel to Z-axis) and transverse component (parallel to Y-axis) of the instantaneous velocity vectors are defined as $u(t)$ and $v(t)$ respectively, and the corresponding mean axial velocity U and transverse velocity V can be quantified by averaging many instantaneous samples. The current study only considered measurement locations where more than 150 valid instantaneous velocity vectors were present, in order to avoid the influence of the jet dynamics, scattering light and smooth surface. The statistical uncertainties of the mean velocity are estimated from the number of validated vectors and standard deviation at each measurement point based on a 95% confidence interval. The maximum measurement uncertainty of U and V is 4% at locations with evident surface deformations, which start from $Z/D = 1$ along the liquid jet surface. Before $Z/D = 1$, the maximum uncertainty can increase to 12% at some locations due to the lack of generated deformed surface features. All the uncertainties are estimated from the number of available vectors and 95% confidence interval, while the relevant uncertainties are listed in Table 3.

3. Results and discussion

In this section, the visual observations of the LJIC based on OC and shadowgraphy are presented in Section 3.1 with the recorded images, which aiming to show the strength of OC on recording the interfacial structures and breakup features of LJIC. Then, the motion of interfacial structures on the liquid jet surface is computed by OFV and the spatial distribution of the interfacial velocities of LJIC is shown in Section 3.2. For the liquid jet breaking in multimode and shear breakup regimes with variable flow conditions, the interfacial velocities of LJIC at different locations are discussed separately based on the gas and liquid interaction and the liquid jet trajectory.

3.1. Liquid jet instantaneous images from OC and shadowgraphy techniques

Fig. 5 presents the OC fluorescent intensity and corresponding shadowgraphic images for all the flow cases of Table 2 observed from the side-view. Shorter liquid jet penetration length can be observed with increasing We_G number for both techniques, and waves, possibly

Table 3
Maximum uncertainties of the mean interfacial velocity for different flow conditions at different regions of the liquid core.

Components Conditions	*Mean axial interfacial velocity*	*Mean transversal interfacial velocity*
Gas flow 3, Group 1&2, at $Z/D < 1$	**7%**	**8%**
Gas flow 3, Group 1&2, at $Z/D > 1$	**4%**	**3%**
Gas flow 4&5, Group 1&2, at $Z/D < 0.8$	**7%**	**7%**
Gas flow 4&5, Group 1&2, at $Z/D > 0.8$	**2%**	**3%**
Gas flow 3, Group 3, at $Z/D < 1.5$	**11%**	**12%**
Gas flow 3, Group 3, at $Z/D > 1.5$	**4%**	**4%**
Gas flow 4&5, Group 3, at $Z/D < 1$	**10%**	**9%**
Gas flow 4&5, Group 3, at $Z/D > 1$	**2%**	**2%**

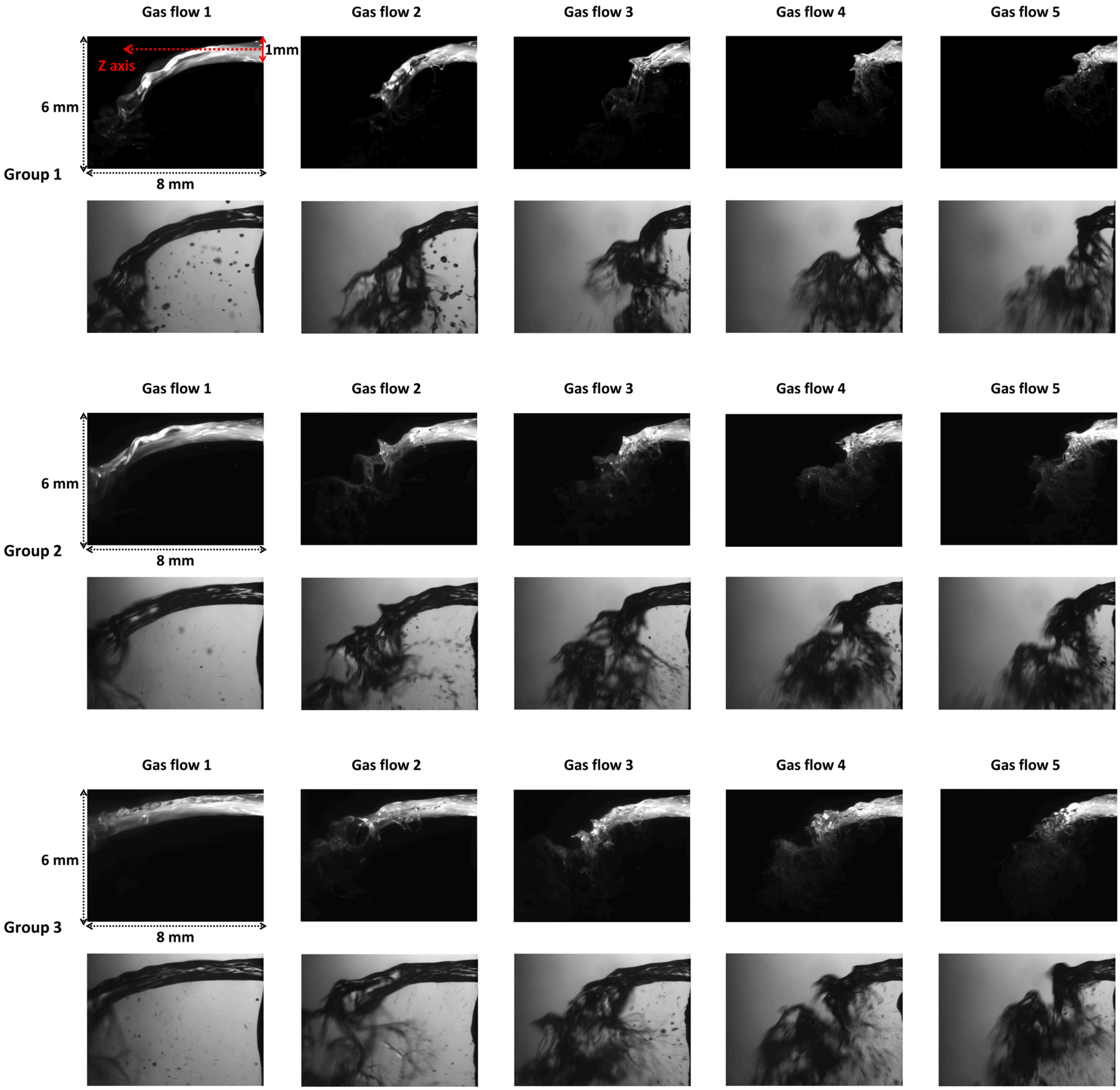

Fig. 5. OC fluorescent intensity images and shadowgraphic images for all flow cases of Table 2; the images from OC are plotted above the corresponding shadowgraphic image.

induced by R-T or/and K-H instabilities, are formed at the windward side of the liquid core. The bag and shear breakup features can be observed in the shadowgraphic images at the relevant breakup regime, which agrees with previous studies of LJIC (Mazallon et al., 1999; Ng et al., 2008; Sallam et al., 2004; Wu et al., 1997). Comparison between OC and shadowgraphic images shows that the surrounding droplet clouds and the stripped-off liquid clusters, as expected, are not recorded on the OC fluorescent intensity images. This is consistent with previous studies when OC was applied to variable types of atomisation processes (Charalampous et al., 2016, 2019;Charalampous et al., 2009; Hadjiyiannis, 2014).

Meanwhile, the optical interference from the stripped-off liquid structures surrounding the continuous liquid core is not a severe problem for OC, even for atomisation under the shear breakup regime, which remains a problem for shadowgraphy. Therefore, the laser light of the OC technique, escaping from the liquid core, is not capable to excite significant levels of fluorescence from the surrounding stripped-off liquid structures which demonstrates the OC advantage in measuring accurately the breakup features of LJIC, such as the breakup height and distance. It is noted that this verification is important, since the liquid jet is bending towards the gas flow direction and the liquid jet surface becomes wavy, which causes some of the laser light rays in the liquid core to escape through the interface, since they are not totally internally reflected on the liquid interface. Downstream of the complete liquid jet break in the gas flow, the light propagation in the liquid core stops and the light diffuses from the breakup point, which may excite fluorescence from some of the surrounding droplets and induce low fluorescent intensity, which can be removed during image processing.

3.2. OC-OFV liquid interface velocity measurements

3.2.1. Interfacial motion of LJIC

The interfacial velocity of the LJIC was computed using OFV as explained in Section 2.3. Many surface features were captured on the liquid jet after the nozzle exit, when the jet is exposed to high-speed gas flow, allowing OFV to measure both the motion of propagating interfacial waves and stripping structures on the liquid jet surface. Velocity vectors calculated from the cross-correlation algorithm were decoupled to *u(t)* and *v(t),* which represents the velocity component associated with the liquid jet injecting direction (positive direction of *Z*-axis) and gas flow direction (negative direction of *Y*-axis) respectively. The instantaneous interfacial velocity *u(t)* and *v(t)* components were locally averaged as *U* and *V* to indicate the averaged interfacial motion on the surface, which are set positive when they are moving along the injection direction of the liquid jet and gas flow. It is noted that the current study only quantified velocity components along the *Z*-axis (*u(t)*) and *Y*-axis (*v (t)*); the velocity component in the *X*-axis cannot be measured

Examples of the measured instantaneous interfacial velocity vector fields for different flow cases are presented in Fig. 6. On the OC fluorescent intensity images, fluorescence with variable intensity can be observed on the jet surface due to the surface wrinkling. By tracing the fluorescent intensities, the movement of the large-scale windward wave and stripping structures at the jet surface can be both quantified and reflected on the vector map. The vector map shows that vectors at regions with smooth surface were rejected by the strict peak ratio criterion, since no variation of fluorescent intensity can be traced and thus no distinct peak can be found in the cross-correlation. Since the stripping surface structures do not have enough time to form immediately after the nozzle exit, the valid velocity vectors close to the nozzle exit are not as dense as at other regions due to the smooth surface. This characteristic is more evident for the liquid jet flow of group 3, which has less

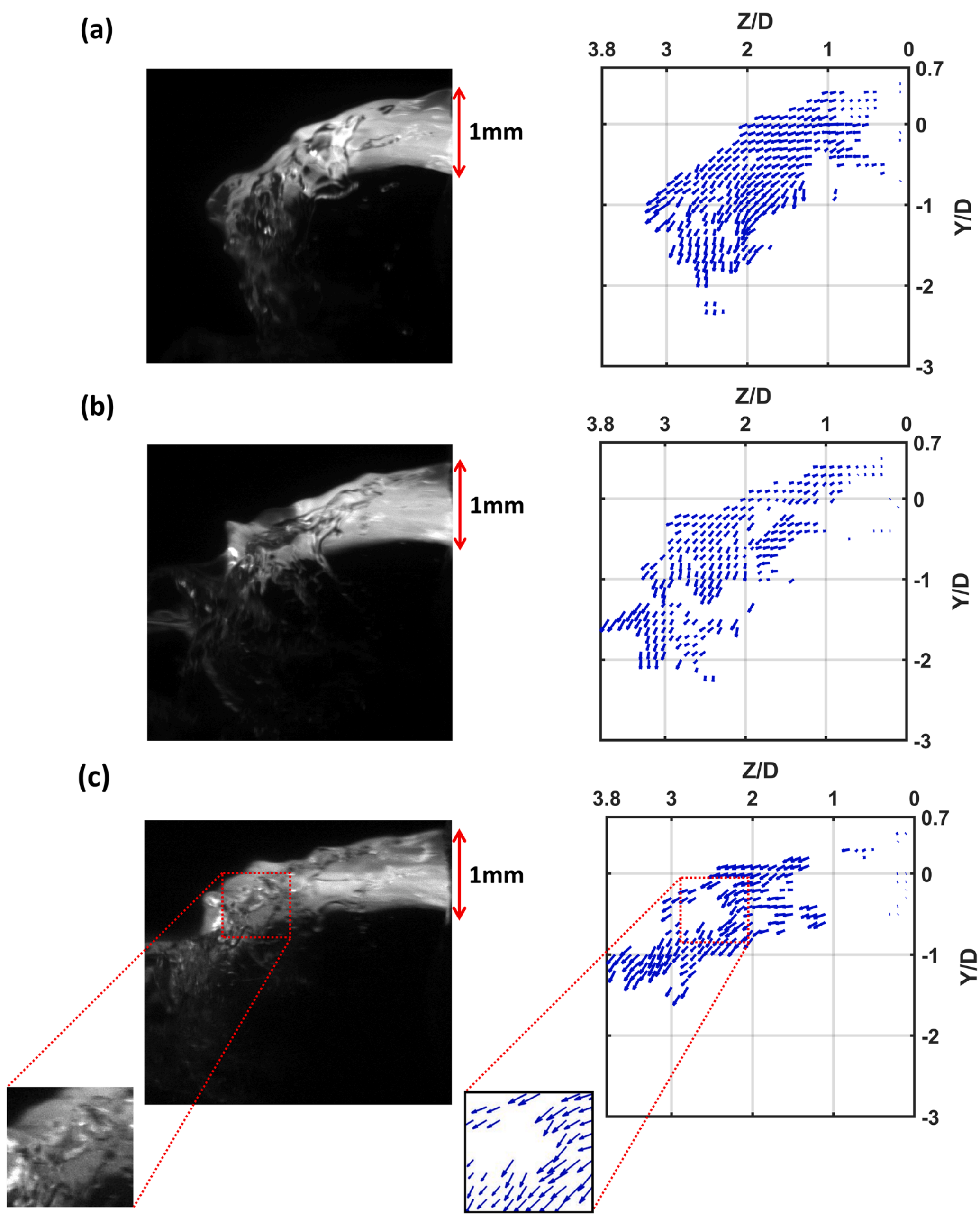

Fig. 6. Examples of the instantaneous velocity vector field and the corresponding OC intensity images. (a) Group 1, gas flow 3; (b) group 2, gas flow 4; (c) group 3, gas flow 5.

velocity vectors close to the nozzle, since the higher liquid jet velocity leads to a longer smooth surface downstream of the nozzle exit. Besides, velocities of some stripping surface structures, attached on the leeward of the jet, such as the stretching ligaments, can also be detected by the OC-OFV technique. The above discussions can be confirmed from Fig. 7, in which the percentage of validated vectors at each point on the surface of LJIC out of 1500 instantaneous images is presented for different flow conditions. At the region close to the nozzle exit, the number of validated vectors is less compared to other regions, as expected. Meanwhile, as discussed previously, for the flow condition of group 3, the liquid jet has higher liquid speed and the region with smooth surface is broader near the nozzle exit (see Fig. 7(c)).

The contour plots of the mean interfacial velocity U and V components are presented in Fig. 8 for flow cases of gas flow 5 from each group of Table 2. The number of detected vectors at locations right after the nozzle exit ($Z/D < 0.5$) is not enough to provide a mean velocity with low uncertainty since the jet surface is smooth and only limited surface structures can be recorded. The statistical uncertainties at these regions increase to 10% relative to that away from the nozzle, which is lower than 5% for a 95% confidence interval. Fig. 8 shows that velocity component U on the windward side of the liquid jet is higher than at the other region and has a strong tendency to increase with distance from the nozzle, especially when the jet starts bending towards the gas flow direction. In addition, the value of U at $Z/D = 1.5$ increases from group 1 (Fig. 8(a)) to group 3 (Fig. 8(c)). As the liquid jet is gradually deflected by the gas flow, the computational work of Li and Soteriou (2016) and PIV measurement of Elshamy et al. (2006), show that the velocity of the deflected gas flow close to the jet surface has initially lower magnitude close to the nozzle exit and increases gradually with the level of bending of the liquid jet and eventually approaches the freestream gas velocity when the liquid jet is fully aligned to the gas flow. Hence, the characteristics of the U velocity component on the windward side are expected, since the injection liquid jet velocity U_L increases from group 1 to 3, and the near surface faster gas flow on the windward side also accelerates the windward interfacial velocity of the liquid jet through aerodynamic shear especially as the liquid jet aligns to the gas flow direction. Moreover, with downstream distance from the nozzle, the U component at the edge and leeward of the jet gradually decreases due to the momentum exchange with the local gas flow. It is noted that the velocity measurements from OC-OFV provide the motion on the 3-D circumference of the liquid jet interface rather than a 2-D observation plane. Therefore, the kinematic characteristics at different regions of the liquid jet surface must be analysed by considering the 3-D interface geometry.

The V velocity component, shown in Fig. 8, initiates from an almost zero magnitude at the windward side, since the liquid jet is injected perpendicularly to the gas flow, and the V component is zero close to the nozzle exit. Then, the V component increases downstream mainly due to jet deflection by the high-speed gas flow. The gaseous shear force surrounding the liquid jet induces a V component to jet surface structures and aerodynamic drag may also contribute to the V component of stripping structures with large dimensions. Therefore, near the tail of the liquid jet, as expected, a higher V is observed due to the more durable gas acceleration. The maximum value of V can be found at the front tip of the liquid jet surface, which may indicate that the gas velocity is higher at this region and the surface structures, therefore, are accelerated further. Therefore, the combined OC-OFV measurements can quantify the interfacial movement of LJIC and explain the development of the interfacial motion of the liquid jet for the first time.

The interfacial velocity of the LJIC, from now on, are decomposed into two categories: windward velocity component U_W and V_W, and surface velocity component U_s and V_s. Fig. 9(a) shows a schematic which is used to denote the velocity categories. The windward velocity U_W and V_W refers to the U and V velocity component at the windward surface of the liquid jet (Fig. 9(a)), indicating the movement of the instability waves or the surface structures at the windward side. Therefore, the current study considered the surface value at the windward side of U and V contour plots, presented in Fig. 8, as U_W and V_W. The windward velocity results from the interaction between the local gas and liquid flow on the windward jet interface, where gaseous shear is imposed on the liquid surface due to the deflected fast gas flow attaching on the windward side of the liquid jet. This is moving slower than V_G before the liquid jet is aligned to the gas flow direction, and gradually accelerating

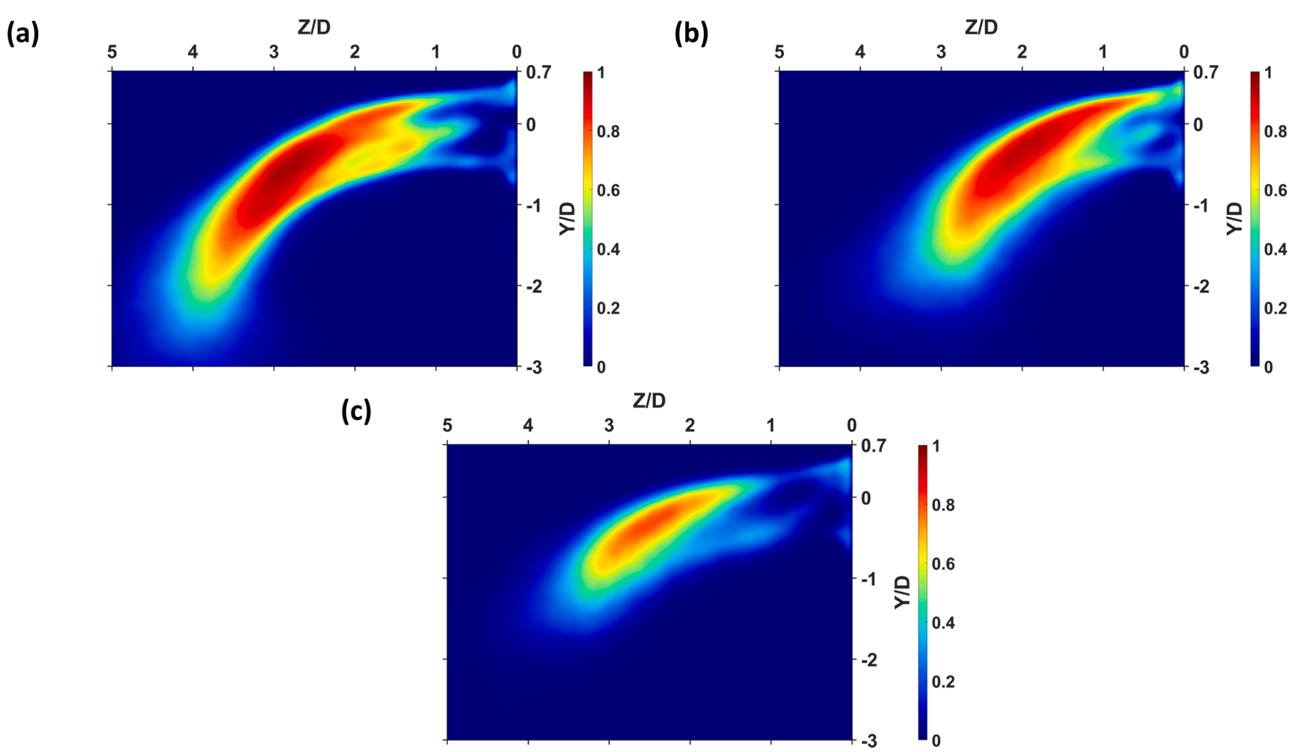

Fig. 7. Percentage of validated vectors along the circumferential surface of LJIC. (a) Group 1, gas flow 3; (b) group 2, gas flow 4; (c) group 3, gas flow 5.

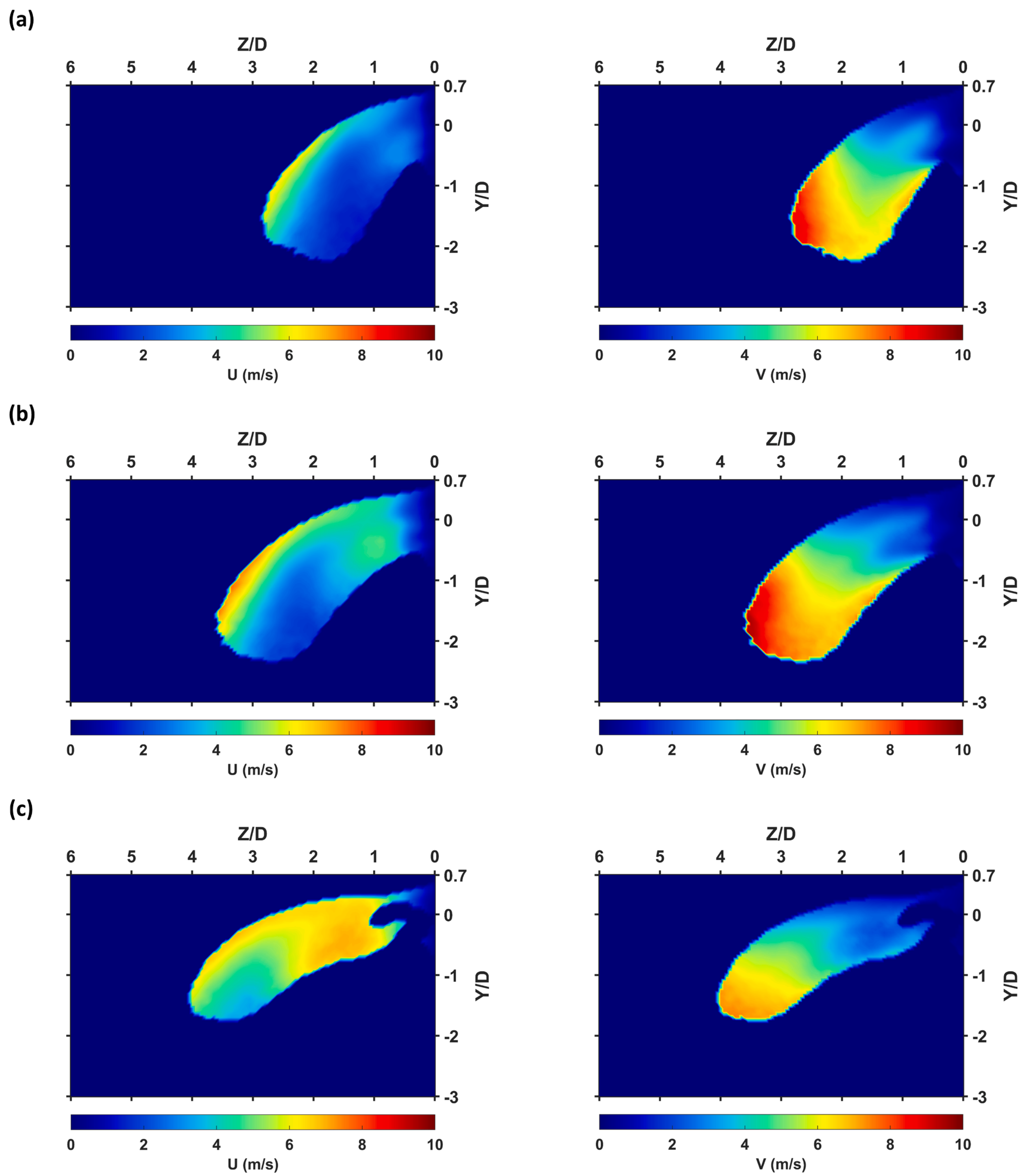

Fig. 8. Contour plots of mean interfacial velocity U (left) and V (right) components. (a) Group 1, gas flow 5; (b) group 2, gas flow 5; (c) group 3, gas flow 5.

the liquid interfacial velocity on the windward side of the jet.

On the other hand, the surface velocity U_s and V_s refers to the U and V velocity components measured from the surface stripping structures surrounding the jet cross-section, as presented in Fig. 9(a) and (b), and include the ligaments at the leeward side of the jet. The quantified surface velocity denotes the motion at the edge of the jet surface, which is mainly induced by the aerodynamic interaction with the high-speed gas flow velocity V_G and local flow variations due to the generated complex flow structures. In the present study, surface velocities cover all the measurable regions except the windward side of the liquid jet which is represented by U_W and V_W. The combined OC-OFV technique velocity measurements can therefore capture the motion of the windward structures and the kinematic characteristics of the stripping surface. The statistical uncertainty of the presented windward and surface velocity is less than 6.3% with 95% confidence interval.

The U component of the windward velocity, U_W, for different flow conditions of each group of Table 2 is shown in Fig. 10. The value of U_W is measured after the nozzle exit and the initial U_W at $Z/D = 0$ is close to

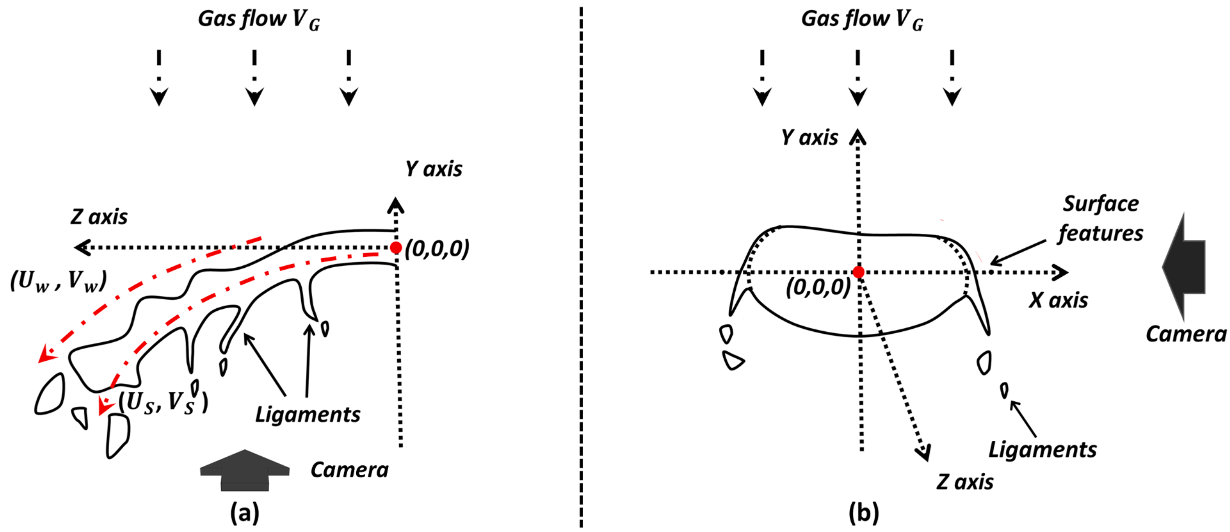

Fig. 9. Schematic of the definition of the two categories of interfacial velocity. (a) Side view of LJIC. (b) A cross-section of LJIC at an axial position along the *Z*-axis of the liquid jet.

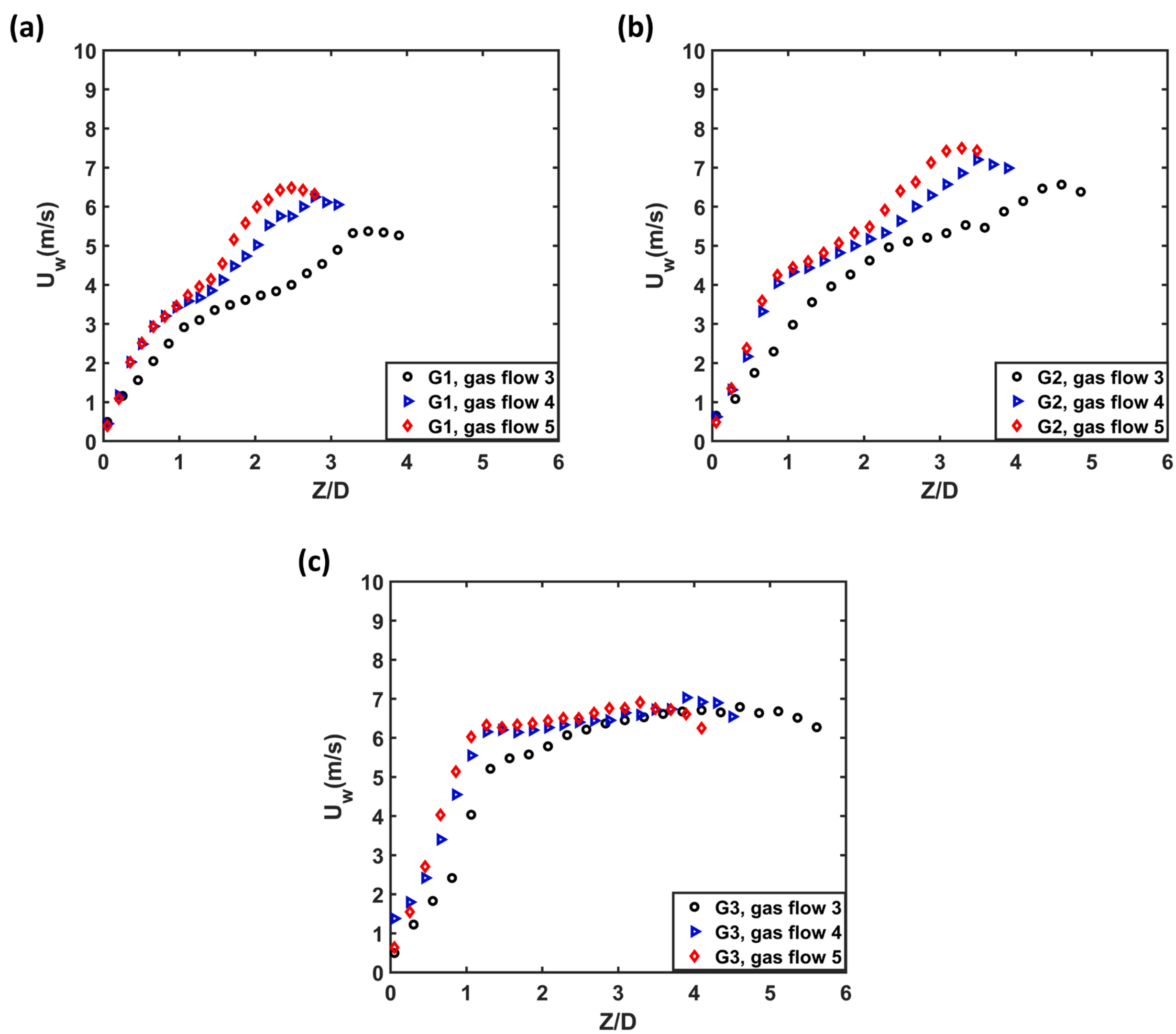

Fig. 10. *U* component of the windward velocity (U_W) for different flow cases of Table 2. (a) Flow cases of group 1; (b) flow cases of group 2; (a) flow cases of group 3.

zero, due to the liquid boundary layer formed on the nozzle wall before the exit. After the liquid exits the nozzle, the free liquid surface changes due to the liquid shear layer relaxation induced by the internal viscous force associated with the sharp velocity gradient under the liquid interface. An acceleration of U_W, hence, can be observed approximately before $Z/D = 1$ for all flow cases. The magnitude of U_W at $Z/D = 1$ is larger for the flow group with a higher U_L (increases from group 1 to 3) and the value of U_W approaches the corresponding injection velocity U_L. Hence, owing to the nozzle length with $L/D = 1.5$, the boundary layer of the liquid jet at the nozzle exit is thin and forms an initial velocity deficit close to the nozzle exit. The liquid velocity acceleration should also be affected by the attaching fast gas flow on the surface at the region before $Z/D = 1$.

Meanwhile, a secondary effect appears to influence the acceleration of U_W after $Z/D = 1$, indicating that the high-speed gas flow on the windward side becomes the main accelerating influence of the jet interface after the viscous force in the liquid shear layer is reduced due to the relaxation of the layer. The development of the U_W along the surface of the jet after around $Z/D = 1$ is mainly determined by the speed of gas flow. U_W for flow cases with faster gas flow is larger and grows faster than the other cases, which is more evident for the cases of groups 1 and 2. This also interprets the slightly stronger growing trend of U_W further away from the nozzle exit (see the profiles after $Z/D = 2$ in Fig. 10(a) and(b)), since the jet at this region is bending further towards the gas flow direction and an increased gas flow shear is generated on the windward surface due to the faster attaching gas flow. For the flow cases of group 3 (Fig. 10(c)), the secondary increasing trend of U_W is not obvious as for the other groups, since the bending of the liquid jet is not distinct which results to a mild gas flow shear. Besides, U_W gradually ceases to increase and becomes constant towards the end of the velocity profile. At this region, the jet approaches breakup, and the tail of the jet interface is almost parallel to the gas flow. The gas flow shear, hence, mainly accelerates the V component of windward velocity rather than the U component at this region.

The measured variable values of U_W with distance from the nozzle do not support the measurements of Ng et al. (2008) and Sallam et al. (2004), who considered that U_W remains equal to U_L at downstream distances from the nozzle. In their experiment, the measurement of U_W was based on double-pulsed shadowgraphic technique and traced the movement of the windward instability wave. The difference between the two measurements is possibly explained by the different types of injection nozzle. The nozzle used by Ng et al. (2008) and Sallam et al. (2004) was a supercavitating nozzle, and thus the initial interfacial velocity may not be influenced by the liquid flow boundary layer at the nozzle wall. In addition, the measurement from their shadowgraphic technique cannot track the development of the interfacial velocity during the

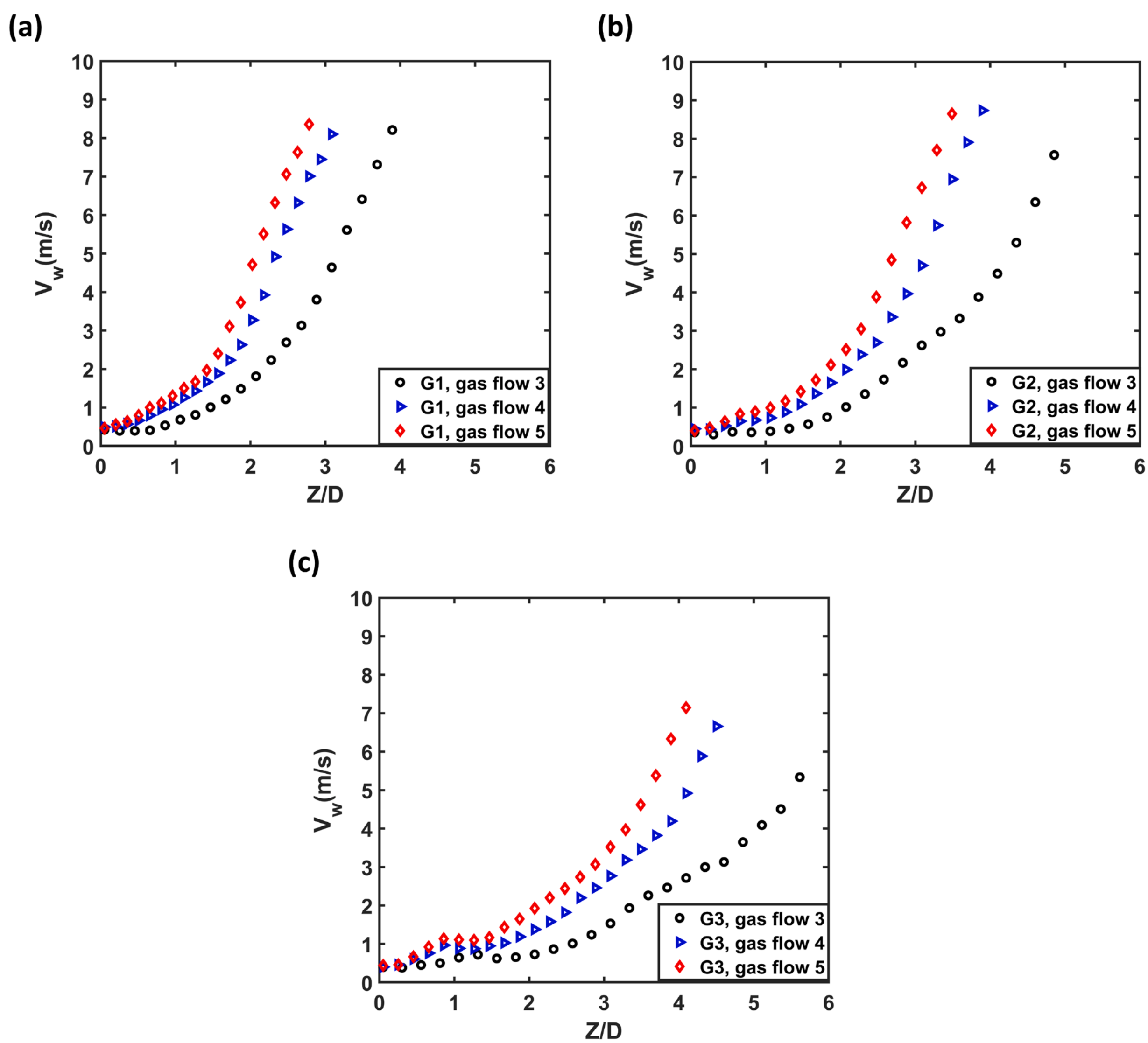

Fig. 11. V component of the windward velocity (V_W) for different flow cases of Table 2. (a) Flow cases of group 1; (b) flow cases of group 2; (c) flow cases of group 3.

entire primary breakup process as the OC-OFV can and leads to U_W measured as being approximately constant, which is avoided by the OC-OFV technique.

The V component of windward interfacial velocity V_W is presented in Fig. 11, which allows comparison with the variation of the U component of Fig. 10. Similarly, as for the U_W, V_W is close to 0 m/s near the nozzle exit, since the initial liquid jet surface has no velocity component along the Y-axis. The measured small initial value of V_W must have been induced by the acceleration from the high-speed gas flow. Moreover, the acceleration of V_W with distance from the nozzle follows a non-linear growth. This characteristic of V_W is consistent with the deflection of the liquid jet, since the acceleration due to the high gas flow shear increases both U_W and V_W, and the further bending of the liquid jet induced stronger shear that accelerates faster the V component. Meanwhile, close to the tail of the liquid jet, the growing trend of V_W becomes more evident due to the described mechanisms, which are also causing the nearly constant U_W values at the tail of the jet, shown in Fig. 10. For flow conditions of the same group, the flow case with faster gas flow has a steeper growth trend in Fig. 11. This can be explained by the higher gas flow shear, which accelerates the liquid jet surface but also bends the jet earlier. The stronger penetration of the liquid jets with higher U_L delays the rapid growth of V_W due to delayed jet deflection, resulting to lower V_W values at the same location compared to the liquid jet with lower U_L for the same gas flow. In general, results from U_W and V_W manifest the development of the windward motion on the liquid jet, demonstrating the interfacial interaction of the two-phase flow. The local geometry of the liquid jet also influences the shear and relevant momentum exchange between the gas and liquid phases.

The surface velocity prescribed in Fig. 9 is also plotted in Fig. 12 for different flow cases. In comparing the development of the surface velocity on the jet surface, two positions along the Y-axis with fixed Z/D values are selected. Positions 1 and 2 are cross-sections along the Y-axis at $Z/D = 1.5$ and $Z/D = 2.5$ respectively. In this way, the streamwise development of the surface velocity on the liquid jet surface can be demonstrated at different locations.

Fig. 12 presents the U component of the surface velocity U_s at the two positions. At position 1, the U_s value increases from group 1 to group 3 due to the higher injection velocity U_L of group 3. For faster gas flow, the U_s of some cases starts to decrease along Y/D, for example, for gas flow 4 and 5 of group 1 and group 2. The decreasing tendency of U_s is linked to the momentum exchange at the stripping structures. The surface structures stripping from the edge of the liquid jet expose the liquid to increased drag induced by the gas flow along the Z-axis, which gradually decreases the magnitude of the U component of the surface velocity. The structures near the windward surface may be influenced by the gas flow acceleration, as discussed for the windward velocity, and acquire higher velocity. Moreover, surface corrugations at the edge of the leeward jet surface may be initially developed from the region close to the nozzle exit and the dimension of these structures could grow during ejection, which provides longer time and stronger drag to decelerate the U component of the surface velocity. Meanwhile, the bending of the liquid jet may also generate higher aerodynamic drag at the edge of the corrugations due to the larger effective area and provide extra time to reduce the U component of the surface structures at the same Z/D position. The above mechanisms explain the decreasing U_s for the faster gas flows of groups 1 and 2, which occurs due to the earlier jet deflection. The decreasing trend of U_s mainly happens at the region away from the windward surface (around $Y/D = -1$ in Fig. 12(a)), since the gas flow attaching on the windward surface will not accelerate the U component at this region and the U component is determined by the deceleration from aerodynamic drag. At the same Z/D position, the surface features on the liquid jet with lower U_L have longer time for the momentum exchange and lead to early decay of U_s along Y/D. Nevertheless, the liquid jet with gas flow 3 for all groups has a stable U_s distribution, which is probably due to the perpendicular jet geometry and small dimension of surface structures, resulting in a shorter time and

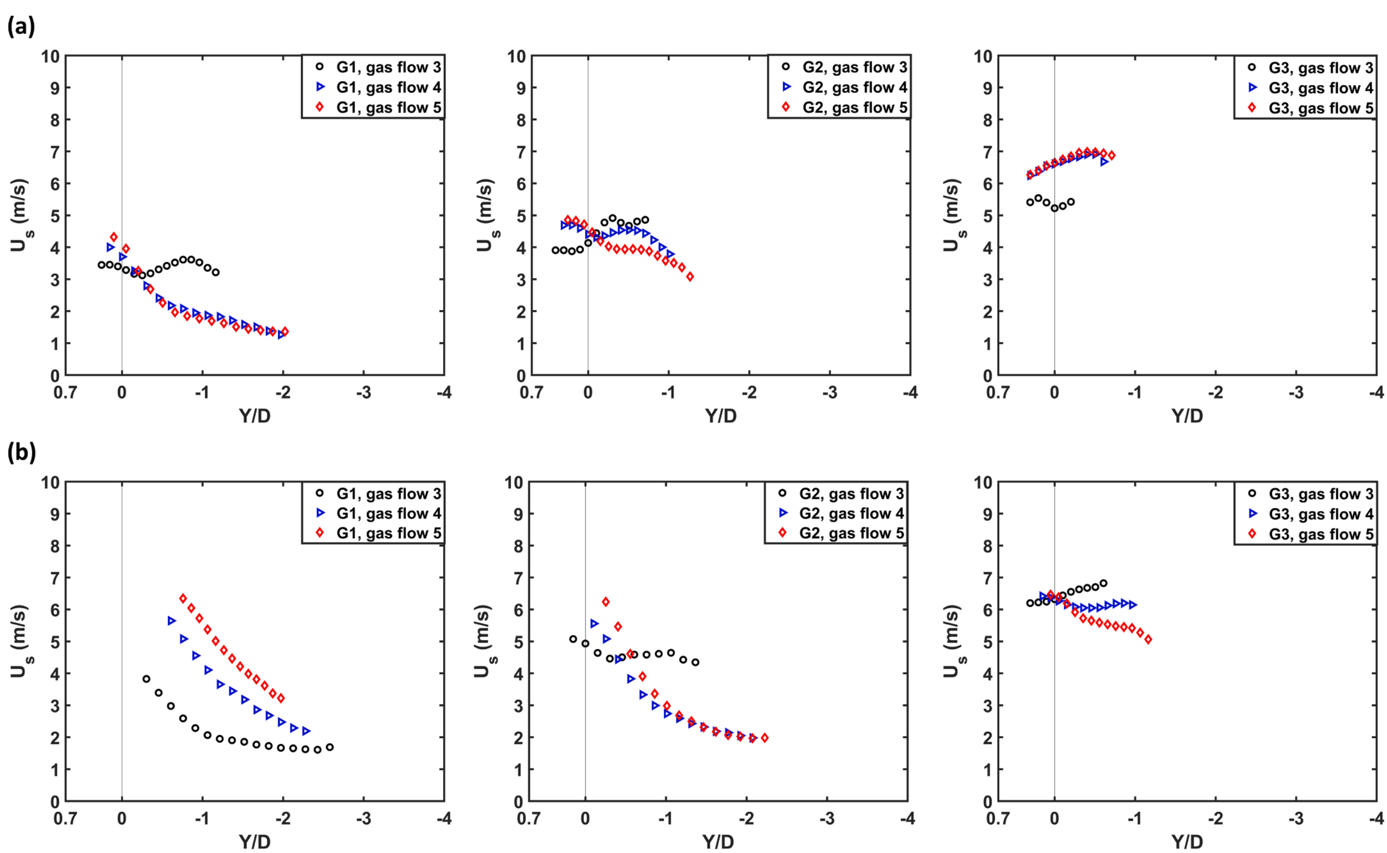

Fig. 12. U component of the surface velocity (U_s) for different flow cases of Table 2. (a) U_s at position 1, along $Z/D = 1.5$; (b) U_s at position 2, along $Z/D = 2.5$.

lower drag during deceleration. This also interprets the flow cases of group 3 for which the U_s values are relatively stable at position 1 for all gas flow cases, since the jet is still straight at $Z/D = 1.5$, and the surface features need more time to develop. However, a slightly increasing trend appears for gas flows 4 and 5, which might be caused by measurement uncertainty or induced by the surrounding flow structures.

For observation position 2 (shown in Fig. 12(b)), the decay of U_s close to the leeward surface is more significant and can be found for almost all flow cases. Even the U_s value of group 3 starts to decrease, since more time and evident jet deflection is provided to slow the U component of the stripping structures, supporting the conclusions for position 1. The initial value of U_s is higher for faster flow cases, which is the result from the windward acceleration and has been discussed for U_w. For the gas flows 4 and 5 of group 1, U_s grows from position 1 to position 2. By observing Fig. 8(a), due to the distinct jet deflection at position 2 for these two flow cases, the U_s values actually represent the accelerated windward velocity U_w and therefore become higher at position 2.

The V component of the surface velocity V_s is plotted in Fig. 13. In contract to U_s, the V_s value always grows along the gas flow direction from the windward velocity V_w, consistent with the observations of Fig. 8. Due to the same mechanism, the gaseous shear and form drag is significant for growing the V_s, which, as expected, is higher for faster gas flow and grows from position 1 to position 2. It is interesting that at position 1, where the detected jet surface is close to the nozzle exit, a near 'step' increase can be observed for V_s (see profiles in Fig. 13(a) of group 2 and group 3). The 'step' increase of V_s can be divided into three segments, namely a primary increase, followed by a relatively stable value and a final secondary growth. The primary increasing segment corresponds to the surface features close to the windward side acquiring V component surface velocity through gas flow interaction, which may eventually become stable around a specific magnitude. Then, at the leeward of the liquid jet, some ligaments (see sketch of Fig. 9) are stripping off from the liquid core and continuously disintegrate to droplets. The motion of these leeward ligaments triggers the secondary growth of V_s since they tend to follow the motion of the fast gas flow and are captured by the OC-OFV technique.

The standard deviation (RMS) of the fluctuations of the instantaneous $v(t)$ and $u(t)$ was also quantified and denoted as u_{RMS} and v_{RMS}. The interfacial turbulent kinetic energy (TKE) of the jet interface, defined by Eq. (3.1), quantifies the magnitude of the fluctuations of the interfacial velocity. It is noted that this definition does not include the third component of the velocity fluctuations, which has not been measured. However, this quantity provides an indication of the magnitude of TKE on the liquid surface for different flow cases and is presented in Fig. 14.

$$TKE = 1/2\left(u_{RMS}^2 + v_{RMS}^2\right) \tag{3.1}$$

At the windward side of the liquid jet, all flow cases have a small magnitude of TKE and indicate that the fluctuations of the velocity of the surface features are small. However, the TKE becomes significant towards the leeward of the liquid jet, while a higher magnitude of TKE can be found at the tip of the liquid trajectory. The motion of the stripping structures at these regions on the liquid jet surface, including ligaments and edge corrugations, are more energetic, since these stripping structures can be easily influenced by the surrounding complex gas flow patterns and thus move randomly. On the other hand, the attached surface features on the edge of the jet surface have a more stable motion.

At the leeward side of the liquid jet, shown in Fig. 14, the location of the TKE maxima varies with gas flow and liquid jet velocity. For a group of flow conditions with a constant U_L, the TKE maxima at the leeward side shift closer to the nozzle exit by increasing the gas flow velocity (from gas flow 3 to 5). This happens because the faster gas flow accelerates the liquid surface quickly (see Fig. 13) and stripping interfacial structures appear closer to the nozzle exit. Since these stripping

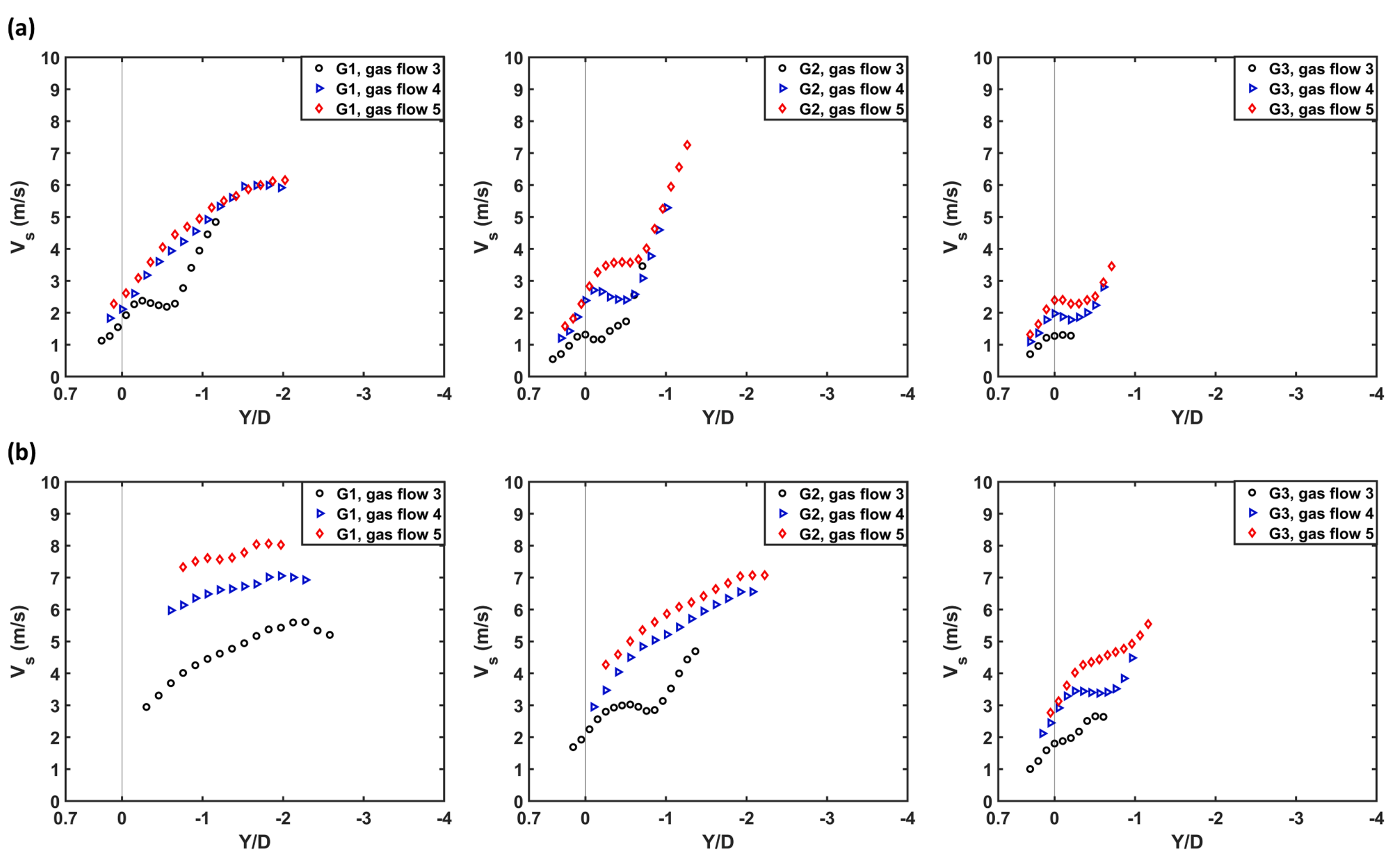

Fig. 13. V component of the surface velocity (V_s) for different flow cases of Table 2. (a) V_s at position 1, along $Z/D = 1.5$; (b) V_s at position 2, along $Z/D = 2.5$.

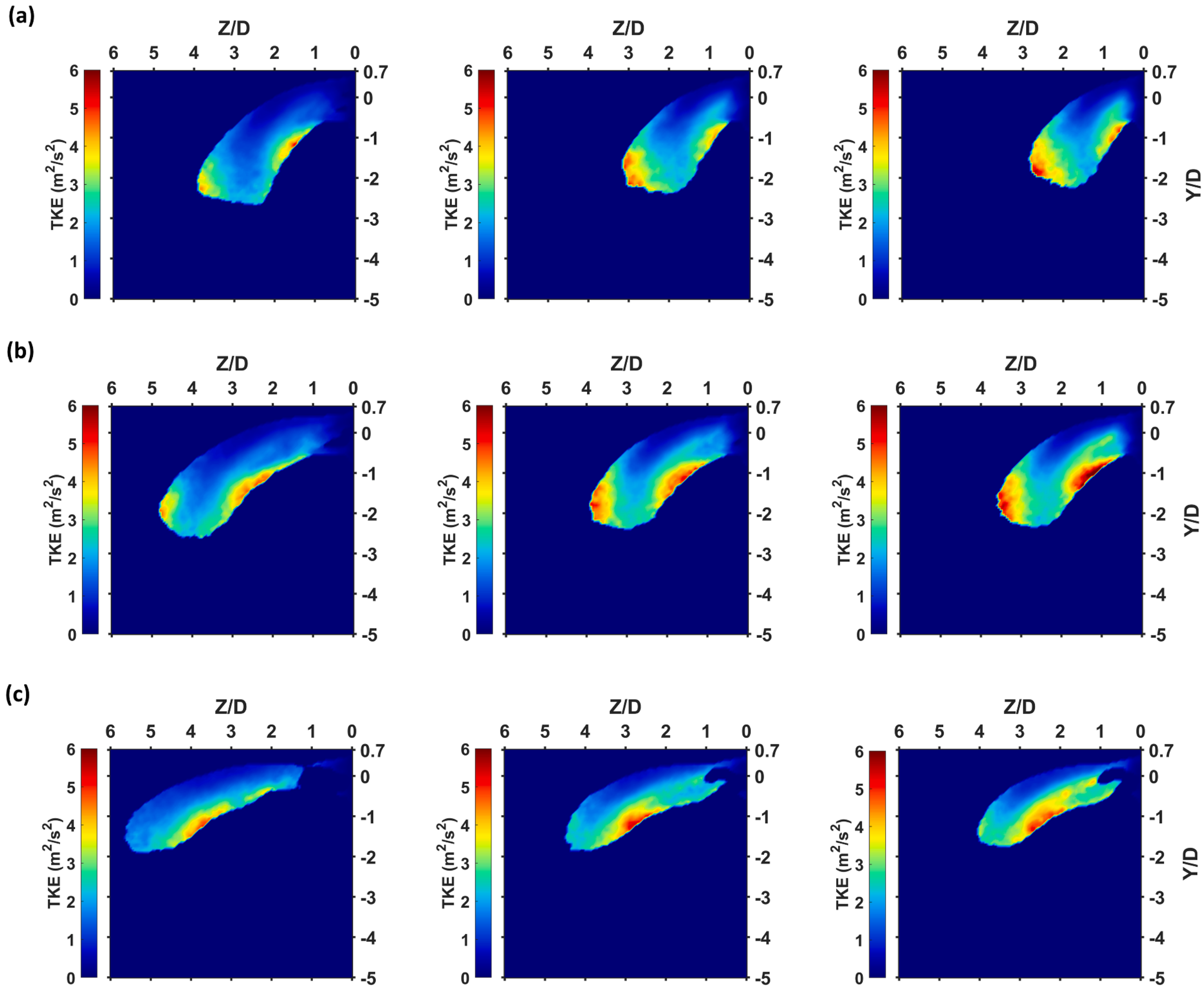

Fig. 14. Interfacial turbulent kinetic energy (TKE) for different flow cases of Table 2, flow cases with gas flow 3 to 5 are shown from left to right in each group. (a) Flow cases of group 1; (b) flow cases of group 2; (c) flow cases of group 3.

interfacial structures are more energetic, the region near the TKE maxima indicates the position where most of the stripping structures can be found. Besides, from group 1 to group 3 under the same gas flow condition, the location of the TKE maxima resides further downstream at the leeward side. The higher U_L from group 1 to group 3 induces the delay of surface peeling at the leeward side since the stripping structures have higher velocity along the *Z*-axis with higher U_L, as shown in Fig. 8. Besides, in the considered flow cases, there is no distinct difference in the magnitude of the TKE maxima at the leeward and tip of the liquid jet.

The u_{RMS} and v_{RMS} values on the surface of the liquid jet were analysed separately. Fig. 15 presents the *RMS* values for flow cases of gas flow 5 from each group of Table 2, same as cases shown in Fig. 8. The u_{RMS} and v_{RMS} for all cases have small magnitude on the windward side, which gradually increases toward the leeward side and tip of the liquid jet. Meanwhile, the magnitude of u_{RMS} is always lower than the corresponding v_{RMS} at the leeward and tip regions, indicating that the complex gas flow at these regions has a stronger effect on the instantaneous $v(t)$. The surrounding gas flow at these regions may contain stronger fluctuating velocities along the gas flow direction that affect the motion of the stripping structures in *Y*-axis. The u_{RMS} and v_{RMS} maxima at the leeward side and tip region, including the unshown cases, have an identical behaviour as the TKE maxima of Fig. 14 and no obvious difference can be identified in their maxima for different flow cases.

In contrast to the leeward side and tip region, for all the presented cases, the u_{RMS} at the windward side shows a higher value than the corresponding v_{RMS}. This can be observed at the region pointed by the red arrow in Fig. 15 and it is more obvious for flow cases in group 3. Besides, under the same gas flow, the u_{RMS} at the windward side slightly increases from group 1 to group 3, while the v_{RMS} values at this region are almost constant. This scenario can also be confirmed by the cases which are not shown here. Since windward velocities mainly represent the motion of interfacial waves initiating from the nozzle exit, the interfacial instabilities may have variable velocity along the *Z*-axis which induces large value of u_{RMS}. From parameters shown in Table 2, u_{RMS} at the windward side is possibly determined by the magnitude of Re_L. An ejecting liquid jet with higher Re_L may have higher fluctuating velocities on the instability waves.

The u_{RMS} and v_{RMS} at the windward surface of the liquid jet, as shown in Fig. 9(a), are presented in Fig. 16 and Fig. 17 respectively. The *RMS* values shown in Fig. 16 and Fig. 17 were measured at the same locations as U_W and V_W presented in Fig. 10 and Fig. 11. From Fig. 16, u_{RMS} at the windward surface for all cases tends to grow with distance from the nozzle exit and remains approximately constant before a rapid increase close to the tip of the liquid jet. In the same group, the liquid jet with faster gas flow always has an early growth after the stable region due to the shorter penetration distance. Meanwhile, from group 1 (Fig. 16(a)) to group 3 (Fig. 16(c)), the rapid growth near the tip region is spatially delayed under the same gas flow velocity, which is caused by the stronger penetration with larger *M*. It is noted that even though the initial u_{RMS} is around 0.5 m/s for all cases, the stable magnitudes of u_{RMS} after the initial growth are different. At $Z/D = 1$, where the initial growth is completed, the u_{RMS} values are roughly identical in the same

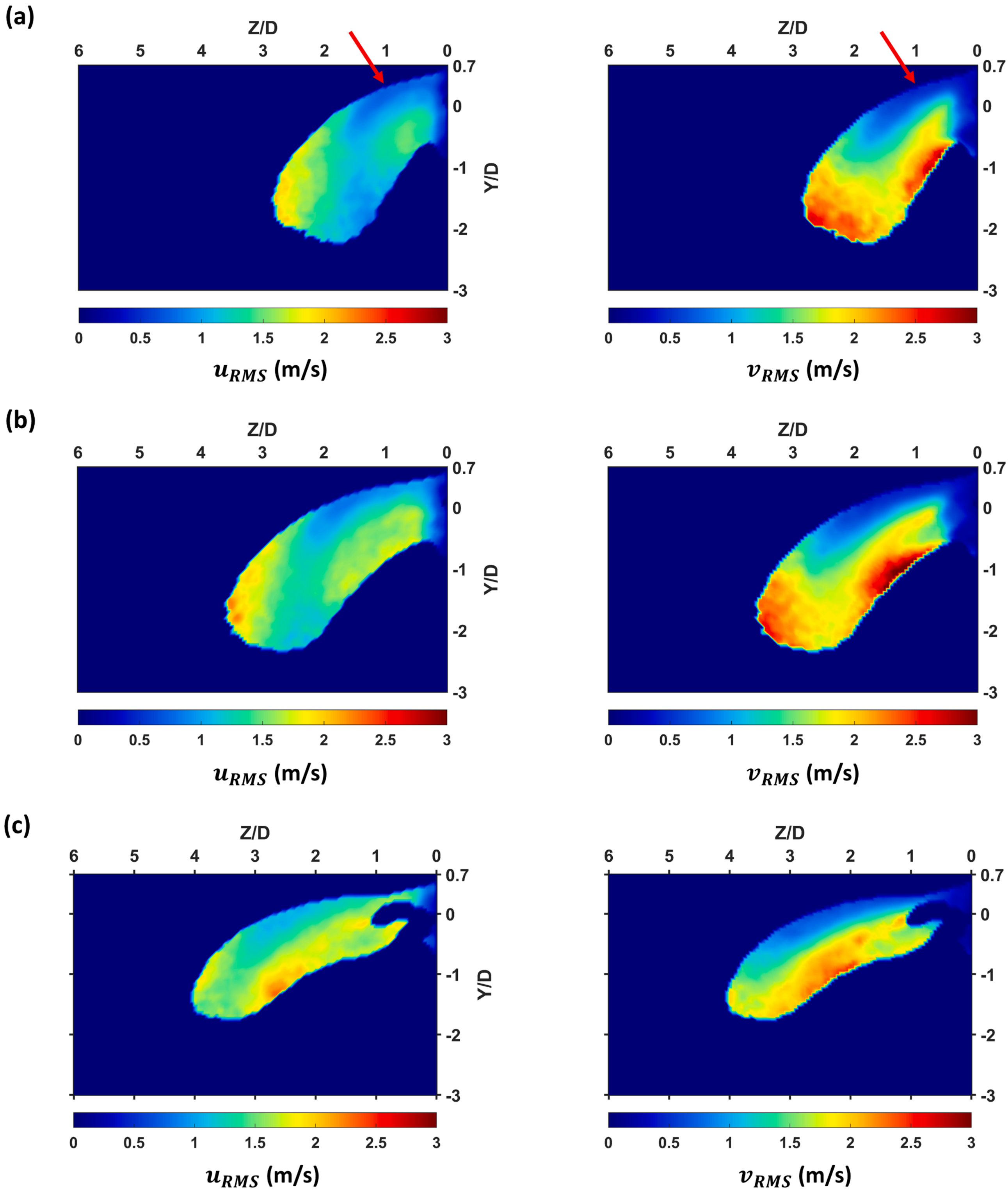

Fig. 15. Contour plots of u_{RMS} (left) and v_{RMS} (right) components. (a) Group 1, gas flow 5; (b) group 2, gas flow 5; (c) group 3, gas flow 5.

group but increase from 0.8 m/s to 1.5 m/s from group 1 to group 3. This result agrees to Fig. 15, in which u_{RMS} values at the windward side are variable between groups and correlate well with Re_L. Besides, a slight decrease of u_{RMS} can be observed after the initial growth for all cases. This may be explained by the bending of the liquid jet during which the velocity fluctuations at the windward surface will be allocated to the *Y*-axis.

The v_{RMS} component at the windward surface of the liquid jet, presented in Fig. 17, has a lower magnitude close to the nozzle exit compared to the corresponding u_{RMS} shown in Fig. 16. The v_{RMS} value close to the nozzle exit is roughly identical across different groups and no obvious growth can be observed at this region as occurs at the corresponding u_{RMS}. Right after the nozzle exit, the v_{RMS} value for all cases starts to increase slowly until the tip region where shows a rapid increase, similar to the corresponding u_{RMS}. The slow increase of v_{RMS} close to the nozzle exit may be dominated by the gas flow velocity, since cases

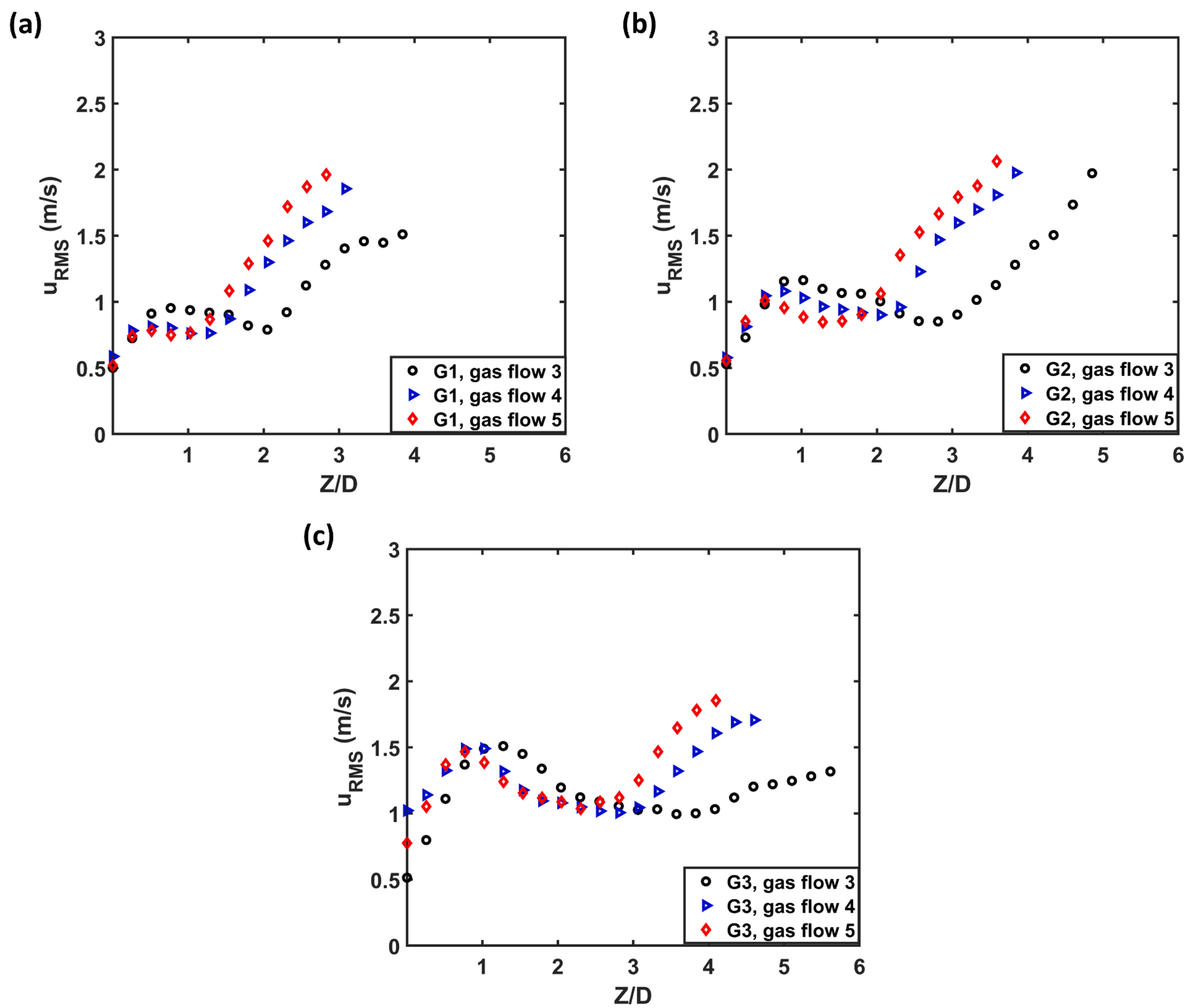

Fig. 16. u_{RMS} component at the windward surface of liquid jet for different flow cases of Table 2. (a) Flow cases of group 1; (b) flow cases of group 2; (a) flow cases of group 3.

with a faster gas flow (for example, the gas flow 5) always have a larger magnitude of v_{RMS} at the same location. This can be explained by the early bending of a liquid jet in a faster gas flow, leading to more velocity fluctuations along the Z-axis which are allocated to the Y-axis component and lead to an early increase of v_{RMS}.

Therefore, the results from Fig. 16 and Fig. 17 classify two regions on the surface depending on the behaviour of *RMS* value of the interfacial velocity fluctuations. The first region includes the tip and leeward of the liquid jet trajectory where interfacial velocity fluctuations are significantly affected by the complex gas flow pattern generated by the gas-liquid interaction. The other region is at the windward surface of the liquid jet where the fluctuations of interfacial velocity are not obvious, and the magnitude of the *RMS* may be determined by the liquid jet velocity U_L and the value of the corresponding Re_L.

The current measurements based on the combined OC-OFV techniques demonstrated the local interfacial motion of the LJIC during the primary breakup process. Variable effects of the jet trajectory and surrounding gas velocity on the interfacial motion are extracted and relevant parameters are quantified. The measured interfacial velocities, including the mean and fluctuating components, reveal the detailed characteristics of the movement of the surface structures and the gas-liquid interaction on the liquid jet surface during the primary breakup, which ultimately determine the initial and downstream motion of the stripping-off droplets and the size and spatial distribution of the downstream droplets of the LJIC. For instance, the velocity distribution of the downstream droplets is probably related to the interfacial windward and surface velocity along the Z direction (U_w and U_s). Besides, this interfacial kinematic information including both the mean and fluctuating components may shed some light on the local mixing process of liquid fuel vapour and air in combustion applications.

4. Conclusions

The current study conducted a liquid jet in crossflow (LJIC) experiment that was operated at different gas Weber numbers and liquid-to-gas momentum flux ratios leading to different breakup regimes, including bag, multimode, and shear breakup regimes. Both shadowgraphy and optical connectivity (OC) techniques were utilized to capture the liquid jet geometry during the primary breakup process, which demonstrated the potential advantages of OC in measuring accurately the breakup characteristics and the liquid jet surface features.

The combined Optical Connectivity and Optical Flow Velocimetry (OC-OFV) techniques measured the interfacial velocity vector of the circumferential surface structures of the LJIC. This experiment, for the first time, quantified the spatial distribution of the interfacial velocity of the continuous liquid core in a high-speed gaseous crossflow. The results show that the interfacial velocity varies with the location of the surface, for example, the development of the interfacial velocity at the windward side and edge side of the jet surface is different. This happens due to the jet trajectory and corresponding distribution of surrounding gas

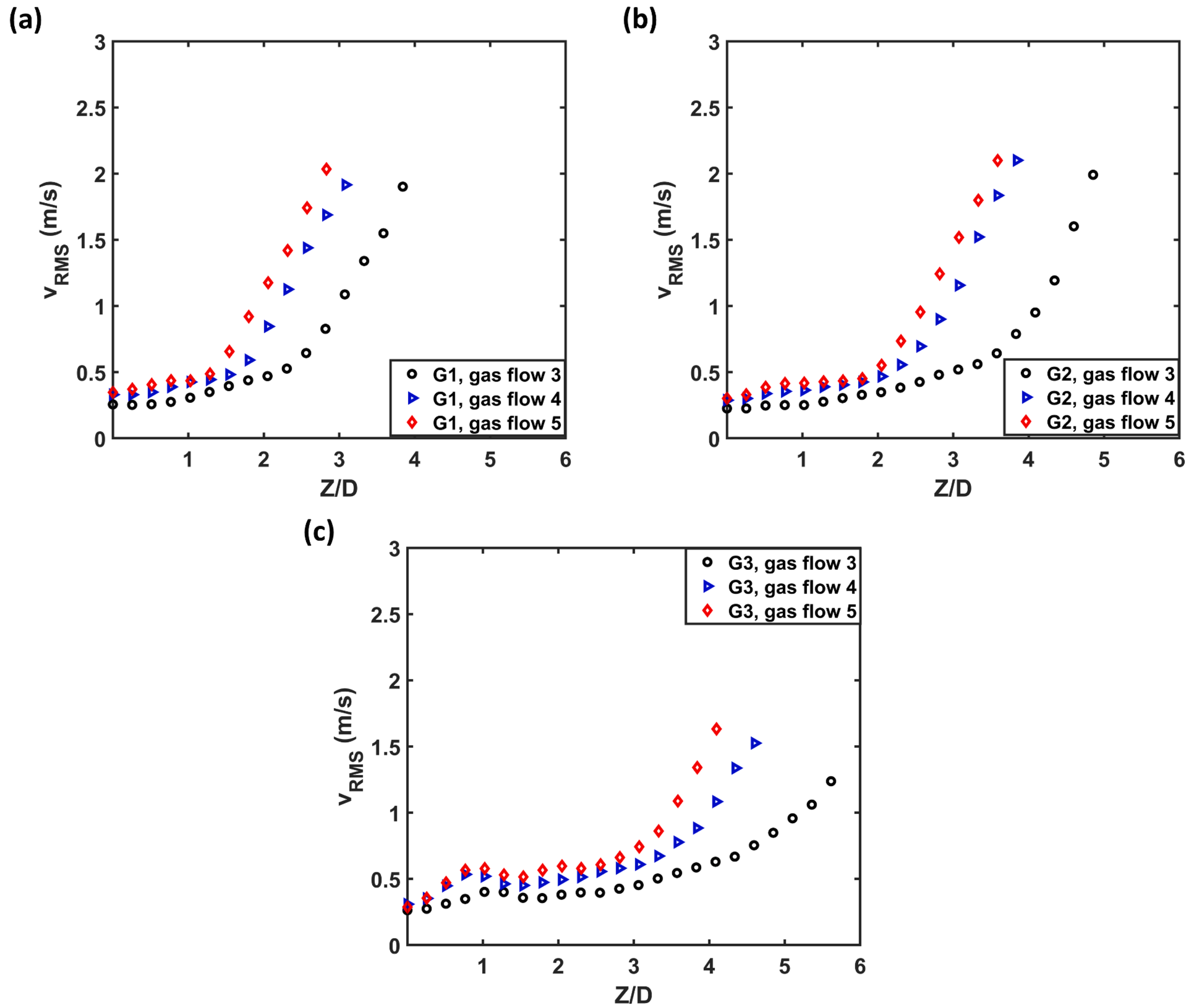

Fig. 17. v_{RMS} component at the windward surface of liquid jet for different flow cases of Table 2. (a) Flow cases of group 1; (b) flow cases of group 2; (a) flow cases of group 3.

velocity, which generates different gas flow interaction along the circumference of the liquid jet.

The development of the interfacial velocity at the windward side is associated with the deflection of the liquid jet by the gas crossflow. The interaction of the liquid jet trajectory with the local gas velocity close to the surface generates different level of gas shear on the windward side of the liquid jet, which determines the spatial development of two components of the interfacial velocity associated with different liquid surface structures.

The velocity at the edge side of the jet surface is also affected by the gas shear from the high-speed gas flow. The influence of aerodynamics drag on the surface structures becomes dominant during the jet deflection and gradually reduces the interfacial velocity component along the liquid jet direction. The velocity component along the gas flow direction, as the interfacial velocity at the windward side of the jet surface, is accelerated by the gaseous shear and may reach a stable value until the surface structures start to strip-off from the leeward side of the jet and follow the motion of the surrounding high-speed gas flow.

Meanwhile, the interfacial velocity has higher fluctuations at the regions where surface structures are stripping off, for example, the tail and the leeward side of the liquid jet, due to the effect of the complex gas flow structures at these regions. The fluctuations at the windward side of the liquid jet, on the other side, may be dominated by the liquid jet velocity U_L and the corresponding liquid Reynolds number Re_L. When the liquid jet is injected with a higher U_L and Re_L, the instability waves at the windward side of the liquid jet contain a wider range of velocities.

In general, the interfacial velocity is important for the application of the LJIC, since it potentially indicates the initial velocity of stripped liquid plumes or droplets from different locations of the jet surface during the primary breakup and explain the spatial distribution of downstream spray droplets during the secondary breakup. The detailed interaction between the gas flow and liquid jet during the primary breakup of LJIC can also be revealed by the measured interfacial kinematic information.

CRediT authorship contribution statement

Tianyi Wang: Conceptualization, Methodology, Validation, Formal analysis, Investigation, Writing – original draft, Visualization. **Yannis Hardalupas:** Writing – review & editing, Supervision, Funding acquisition, Resources, Project administration.

Declaration of Competing Interest

The authors declare that they have no known competing financial interests or personal relationships that could have appeared to influence the work reported in this paper.

Data availability

Data will be made available on request.

Acknowledgments

The authors would like to acknowledge support from the Engineering and Physical Sciences Research Council (EPSRC) through grants EP/G01597X/1 and EP/W016265/1.

References

Adrian, L., Adrian, R.J., Westerweel, J., 2011. Particle Image Velocimetry. Cambridge university press.

Arienti, M., Soteriou, M.C., 2009. Time-resolved proper orthogonal decomposition of liquid jet dynamics. Phys. Fluids 21 (11), 112104.

Behzad, M., Ashgriz, N., Karney, B., 2016. Surface breakup of a non-turbulent liquid jet injected into a high pressure gaseous crossflow. Int. J. Multiphase Flow 80, 100–117.

Birouk, M., Azzopardi, B.J., Stäbler, T., 2003. Primary Break-up of a viscous liquid jet in a cross airflow. Particle & Particle Syst. Characterization: Measurement and Description of Particle Properties and Behav. Powders and Other Disperse Syst. 20 (4), 283–289.

Broumand, M., Birouk, M., 2016. Liquid jet in a subsonic gaseous crossflow: recent progress and remaining challenges. Progress in Energy and Combustion Sci. 57, 1–29.

Broumand, M., Birouk, M., 2019. Liquid jet primary breakup in a turbulent cross-airflow at low Weber number. J. Fluid Mech. 879, 775–792.

Charalampous, Hardalupas, Y, 2016. How do liquid fuel physical properties affect liquid jet development in atomisers? Phys. Fluids 28 (10), 102106.

Charalampous, G., Hadjiyiannis, C., Hardalupas, Y., 2016. Comparative measurement of the breakup length of liquid jets in airblast atomisers using optical connectivity, electrical connectivity and shadowgraphy. Measurement 89, 288–299.

Charalampous, G., Hadjiyiannis, C., Hardalupas, Y., 2019. Proper orthogonal decomposition of primary breakup and spray in co-axial airblast atomizers. Phys. Fluids 31 (4), 043304.

Charalampous, G., Hardalupas, Y., Taylor, A., 2007. A novel technique for measurements of the intact liquid jet core in a coaxial airblast atomizer. In: Paper presented at the 45th AIAA Aerospace Sciences Meeting and Exhibit.

Charalampous, G., Hardalupas, Y., Taylor, A., 2009. Novel technique for measurements of continuous liquid jet core in an atomizer. AIAA J. 47 (11), 2605–2615.

Elshamy, O., Tambe, S., Cai, J., Jeng, S.M., 2006. Structure of liquid jets in subsonic crossflow at elevated ambient pressures. In: Paper presented at the 44th AIAA Aerospace Sciences Meeting and Exhibit.

Fielding, J., Long, M.B., Fielding, G., Komiyama, M., 2001. Systematic errors in optical-flow velocimetry for turbulent flows and flames. Appl. Optics 40 (6), 757–764.

Ghosh, S., Hunt, J., 1998. Spray jets in a cross-flow. J. Fluid Mech. 365, 109–136.

Hadjiyiannis, C., 2014. PhD thesis. Imperial College London.

Kelso, R.M., Lim, T., Perry, A., 1996. An experimental study of round jets in cross-flow. J. Fluid Mech. 306, 111–144.

Komiyama, M., Miyafuji, A., Takagi, T., 1996. Flamelet behavior in a turbulent diffusion flame measured by Rayleigh scattering image velocimetry. Paper Presented at the Symposium (International) on Combustion.

Lee, K., Aalburg, C., Diez, F.J., Faeth, G.M., Sallam, K.A., 2007. Primary breakup of turbulent round liquid jets in uniform crossflows. AIAA J. 45 (8), 1907–1916.

Li, X., Soteriou, M.C., 2016. High fidelity simulation and analysis of liquid jet atomization in a gaseous crossflow at intermediate Weber numbers. Phys. Fluids 28 (8), 082101.

Li, X., Soteriou, M.C., 2018. Detailed numerical simulation of liquid jet atomization in crossflow of increasing density. Int. J. Multiphase Flow 104, 214–232.

Linne, M.A., Paciaroni, M., Gord, J.R., Meyer, T.R., 2005. Ballistic imaging of the liquid core for a steady jet in crossflow. Appl. Optics 44 (31), 6627–6634.

Lubarsky, Reichel, J.R., Zinn, B.T., McAmis, R, 2010. Spray in crossflow: dependence on Weber number. J. Eng. Gas Turbines and Power 132 (2).

Lubarsky, E., Shcherbik, D., Bibik, O., Gopala, Y., Zinn, B., 2012. Fuel jet in cross flow—experimental study of spray characteristics. Advanced Fluid Dynamics, p. 59.

Mahesh, K., 2013. The interaction of jets with crossflow. Ann. Rev. Fluid Mech. 45, 379–407.

Mazallon, J., Dai, Z., Faeth, G., 1999. Primary breakup of nonturbulent round liquid jets in gas crossflows. Atomization and Sprays 9 (3).

Ng, C.L., Sankarakrishnan, R., Sallam, K., 2008. Bag breakup of nonturbulent liquid jets in crossflow. Int. J. Multiphase Flow 34 (3), 241–259.

Osta, A., Sallam, K., 2007. Effect of nozzle length/diameter ratio on the breakup of liquid jets in crossflow. In: *APS, 60*, GC. 003.

Raffel, M., Willert, C.E., Scarano, F., Kähler, C.J., Wereley, S.T., Kompenhans, J., 2018. Particle Image Velocimetry: A Practical Guide. Springer.

Sallam, K., Aalburg, C., Faeth, G., 2004. Breakup of round nonturbulent liquid jets in gaseous crossflow. AIAA J. 42 (12), 2529–2540.

Sallam, K., Dai, Z., Faeth, G., 2002. Liquid breakup at the surface of turbulent round liquid jets in still gases. Int. J. Multiphase Flow 28 (3), 427–449.

Sallam, K., Ng, C., Sankarakrishnan, R., Aalburg, C., Lee, K., 2006. Breakup of turbulent and non-turbulent liquid jets in gaseous crossflows. In: Paper presented at the 44th AIAA Aerospace Sciences Meeting and Exhibit.

Sedarsky, D., Gord, J., Carter, C., Meyer, T., Linne, M., 2009. Fast-framing ballistic imaging of velocity in an aerated spray. Optics Lett. 34 (18), 2748–2750.

Sedarsky, D., Idlahcen, S., Rozé, C., Blaisot, J.B., 2013. Velocity measurements in the near field of a diesel fuel injector by ultrafast imagery. Experiments in Fluids 54 (2), 1451.

Seuntiëns, H., Kieft, R., Rindt, C., Van Steenhoven, A., 2001. 2D temperature measurements in the wake of a heated cylinder using LIF. Experiments in Fluids 31 (5), 588–595.

Tokumaru, P., Dimotakis, P., 1995. Image correlation velocimetry. Experiments in Fluids 19 (1), 1–15.

Wang, T., Hardalupas, Y., 2021. Combined optical connectivity and optical flow velocimetry for interfacial characterisation of liquid atomisation. In: Paper presented at the International Conference on Liquid Atomization and Spray Systems (ICLASS).

Wu, P.K., Kirkendall, K.A., Fuller, R.P., Nejad, A.S., 1997. Breakup processes of liquid jets in subsonic crossflows. J. Propulsion and Power 13 (1), 64–73.

Wu, P.K., Kirkendall, K.A., Fuller, R.P., Nejad, A.S., 1998. Spray structures of liquid jets atomized in subsonic crossflows. J. Propulsion and Power 14 (2), 173–182.